ABSTRACT

Title of dissertation: THE RESPONSE OF MOLECULAR GASES AND MODULATED PLASMAS TO SHORT INTENSE LASER PULSES

Andrew James Pearson
Doctor of Philosophy, 2011

Dissertation directed by: Professor Thomas Antonsen
Department of Physics

In this thesis we study the response of two systems to short, intense laser pulses. The first system is a gas of diatomic molecules whose ensemble-averaged alignment features rotational revivals. We analyze the effect of a background plasma on the revival peaks. Both the revivals and the plasma are the result of a laser pulse passing through the gas. The second system is a density-modulated plasma channel. We study the generation of electromagnetic radiation by a laser pulse passing through this structure.

The molecules in the gas are modeled as rigid rotors that interact first with the cycle-averaged electric field of the laser pulse, and second with the fluctuating electric field of the background plasma. The laser pulse generates a broad superposition of angular momentum eigenstates, resulting in the transient alignment of the molecules. Because of the time evolution properties of the angular momentum states, the alignment re-occurs periodically in field-free conditions. The alignment is calculated using a density matrix, and the background plasma is modeled using

dressed particles. The result is decoherence between the phases of the basis states of the wavefunction, which causes decay of subsequent alignment peaks. We find that field-induced decoherence is competitive with collisional decoherence for small ionization fractions.

The corrugated plasma channel is modeled using linear plasma theory, and the laser pulse is non-evolving. Corrugated channels support EM modes that have a Floquet dispersion relation, and thus consist of many spatial harmonics with subluminal phase velocities. This allows phase matching between the pulse and the EM modes. Since the pulse bandwidth includes THz frequencies, significant THz generation is possible. Here we consider realistic density profiles to obtain predictions of the THz power output and mode structure. We then estimate pulse depletion effects. The fraction of laser energy converted to THz is independent of laser pulse energy in the linear regime, and we find it to be around one percent. Extrapolating to a pulse energy of 0.5 J gives a THz power output of 6 mJ, with a pulse depletion length of less than 20 cm.

THE RESPONSE OF MOLECULAR GASES AND MODULATED PLASMAS TO SHORT INTENSE LASER PULSES

by

Andrew James Pearson

Dissertation submitted to the Faculty of the Graduate School of the
University of Maryland, College Park in partial fulfillment
of the requirements for the degree of
Doctor of Philosophy
2011

Advisory Committee:
Professor Thomas Antonsen, Chair/Advisor
Professor Howard Milchberg
Professor James Drake
Professor Howard Elman
Assistant Professor Ki-Yong Kim

Acknowledgments

There are many people to whom I am grateful for their support, assistance and encouragement over the past few years.

I'll begin by acknowledging my advisor, Prof. Thomas Antonsen. His door was always open when I had questions, and he always had interesting comments and ideas when progress was not forthcoming. I'd like to thank him for this, for allowing me to work on interesting projects during my time as a graduate student and for tolerating my many visits to Florida. Similar thanks go to Dr. John Palastro, who was also available for discussion and advice whenever needed.

I'd like to express abundent gratitude to my family. My wife has been unconditionally supportive during the time I've known her, and I thank her for all of her love and encouragement. I also thank my parents for their relentless hard work and encouragement for very many years. This support was vital in allowing me to get where I am today. I include here my sister, my parents-in-law, and my brother-in-law and his family for their kind support. Finally, I would be remiss if I failed to mention my cat, Φ.

I conclude by thanking the following people for acts of support: Prof. Howard Milchberg, Prof. James Drake, Asst. Prof. Ki-yong Kim and Prof. Howard Elman for taking the time to be on my committee. Asst. Prof. Eric Brewe and Prof. Laird Kramer of Florida International University for providing office space during my time in Miami. Dr. Nicholas Mecholsky and Dr. Kate Despain for numerous interesting discussions. Tak Chu Li and Wenxi Zhu for sharing my love of coffee.

Table of Contents

List of Tables iv

List of Figures v

1 Introduction 1

2 The Effect of Electric Field Fluctuations on Rotational Revival Amplitudes 4
- 2.1 Introduction . . . 4
- 2.2 Decoherence due to electric field fluctuations . . . 6
- 2.3 Modeling a gas of diatomic molecules . . . 9
  - 2.3.1 Density matrix formalism . . . 9
  - 2.3.2 Molecular alignment by a linearly polarized laser pulse . . . 11
  - 2.3.3 Interaction matrix for a fluctuating background electric field . 13
- 2.4 Numerical Simulation Results . . . 17
- 2.5 Conclusion . . . 29

3 Simulation of THz Generation in Corrugated Plasma Waveguides 31
- 3.1 Introduction . . . 31
- 3.2 Excitation of Modes in a Corrugated Channel . . . 33
  - 3.2.1 Requirements for Excitation . . . 33
  - 3.2.2 Parabolic Plasma Channels . . . 35
  - 3.2.3 Finite Radius Plasma Channels . . . 39
- 3.3 Code Details and Verification . . . 41
  - 3.3.1 Model and Assumptions . . . 41
  - 3.3.2 Algorithm . . . 51
  - 3.3.3 Implementation . . . 53
  - 3.3.4 Post-Processing . . . 55
  - 3.3.5 Code Verification . . . 57
- 3.4 Simulation Results . . . 61
- 3.5 Conclusion . . . 76

A Calculating the Approximate Dispersion Relation 79

Bibliography 83

List of Tables

3.1 Values of the difference between power input and output ΔP, and the radial power flow $\langle P_r \rangle$, for the different scenarios in Fig. 3.6. For comparison, the result for a full-strength ($\delta = 0.9$) channel is listed. . 61

3.2 Values of energy emitted in THz radiation and laser pulse depletion length for two different values of pulse energy and various mode widths. These quantities are calculated for a density of 1.3×10^{18} cm^{-3}, corresponding to peaks in Fig. 3.7(c). 64

List of Figures

2.1 Ensemble average alignment vs. time calculated in the zero-pulse-length limit. Plot domain includes the laser pulse at $t = 0$ and the first full revival at $t = \tau_R$. Note that the first peak of the alignment occurs after the laser pulse, due to the characteristic response time of the molecules. This feature is preserved in short, finite-length pulses. 13

2.2 Ensemble-averaged alignment as a function of time for HCN molecules in a plasma with room temperature ions. In (a) the interaction considered is the permanent dipole, the plasma density is $n = 10^{18}$ cm^{-3} and the electron temperature is T_e =1 eV. In (b), the electron temperature has been increased to T_e =10 eV. In (c) the interaction considered is the permanent quadrupole, the plasma density has increased $n = 10^{19}$ cm^{-3} and the electron temperature is once again T_e =1 eV, while in (d) the interaction considered is the induced dipole, the plasma density is $n = 10^{20}$ cm^{-3} and the electron temperature is T_e =1 eV. 20

2.3 Ensemble-averaged alignment as a function of time for N_2 molecules in a plasma with room temperature ions. In (a) the interaction considered is the permanent quadrupole, the plasma density is $n = 10^{19}$ cm^{-3} and the electron temperature is T_e =1 eV. In (b), the electron temperature has been increased to T_e =10 eV. In (c) the interaction considered is the induced dipole, the plasma density has increased $n = 10^{20}$ cm^{-3} and the electron temperature is once again T_e =1 eV. 22

2.4 Variation of decay time with system parameters. In (a), we show the decay time as a function of ion velocity, with fixed density $n = 10^{18}$ cm^{-3}. The temperature associated with the angular momentum population distribution was fixed at 300 K. In (b), we show the decay time as a function of density, with room temperature ions. In both cases, the electron temperature is fixed at 10 eV. 24

3.1 (a) Diagram of experimental setup for producing a corrugated plasma channel. As an alternative to a spatially modulated formation pulse, a modulated cluster density may be used in conjunction with a uniform formation pulse. (b) Dispersion plot of EM modes in the delta function corrugated channel (considered by Antonsen et. al.) which consists of a channel with a density profile that has a train of delta functions, thus creating a period system while allowing the use of analytic results from the axially uniform case. Here, d is the distance between consecutive delta functions, while ω and k_c are the frequency and wavenumber. 32

3.2 Plot of normalized bandgap size as a function of normalized central bandgap frequency, obtained from the numerical calculation of the dispersion relation, performed in the Appendix. Note that the bandgap size vanishes rapidly with increasing frequency, at a point far below the typical frequencies associated with an optical pulse. . . 48
3.3 Plots of the Fourier transforms of 50 fs laser pulses with wavelength 800 nm and spot size 15 μm, recorded initially (blue) and after propagation for 40 Rayleigh lengths for normalized vector potential amplitudes of (a) $a_0 = 0.2$, (b) $a_0 = 0.4$ and (c) $a_0 = 0.8$. These potentials correspond to pulse energies of 0.03, 0.1 and 0.5 J respectively. Plot (d) is for $a_0 = 0.8$ for a pulse propagating over one Rayleigh length. These plots were generated using the simulation WAKE. 50
3.4 Stability surface cross sections evaluated at $k_z\Delta z = \pi$ for the eigenvalue associated with $E_x^{n-\frac{1}{2}}$ of the amplification matrix for a Cartesian two-dimensional Maxwell-Fluid system without damping. We have (a) $dt = dt_{CFL}$, (b) $dt = 0.95\,dt_{CFL}$ and (c) $dt = 0.9\,dt_{CFL}$. . . . 53
3.5 Plots from a simulation of a laser pulse passing through a uniform plasma showing (a) density perturbation $\delta n/n_0$ calculated analytically (blue line) and numerically (red circles) for a uniform plasma and (b) difference between power input and output as a function of normalized stepsize squared. Plots of $\widetilde{E}_z(k_z, \omega)$ from a simulation of a laser pulse passing through a parabolic plasma channel evaluated for (c) $v_g = c$ at $r = 0$ and (d) for $v_g = 2c$ at $r > r_0$. 57
3.6 Axial and radial power flow density in frequency space for (a) uniform plasma, (b) $\delta = 0.05$ axial corrugations but no radial density dependence, (c) a finite radius plasma channel with no axial corrugations and (d) a finite radius plasma channel with $\delta = 0.05$ axial corrugations. 59
3.7 Plots involving various quantities as a function of density for channel widths $w_{ch} = 15$ μm (blue, solid), $w_{ch} = 25$ μm (red, dashed), $w_{ch} = 50$ μm (green, dash-dot) and $w_{ch} = 75$ μm (magenta, dotted). The quantities are (a) average power flow in the radial direction, (b) average power flow in the axial direction, (c) percentage of laser energy converted to THz and (d) angle between the Poynting vector measured outside the channel and the axis. 62
3.8 Plots involving various quantities as a function of pulse duration for density $n_0 = 1.25 \times 10^{18}$ cm^{-3} and channel width $w_{ch} = 25$ μm. The quantities are (a) average power flow in the radial direction, (b) average power transferred from the laser pulse to the plasma, (c) percentage of laser energy converted to THz and (d) average power transferred from the laser pulse to the plasma rescaled for fixed peak ponderomotive potential. Note that at $\tau = 50$ fs, these quantities do not match the results in Fig. 3.7 because the simulation length was shorter, and the damping rate ν was necessarily larger. 68

3.9 Average radial power spectral density for different cutoff radii and for corrugated channels with mode width (a) $w_{ch} = 15$ μm and (b) $w_{ch} = 50$ μm. The topmost plots have $r_c = 1.5w_{ch}$, and the cutoff radius increases by $.5w_{ch}$ for each successive plot. The subfigure to the right of each power plot displays a z-averaged radial density profile. 70
3.10 Two-dimensional Fourier transforms of E_z taken at fixed radius outside the channel for (a) $w_{ch} = 15$ μm and (b) $w_{ch} = 50$ μm. The red (solid) line is the lightline of the laser pulse, and the blue (dotted) curves are the functions in Eq. (3.10) that constitute the approximate dispersion relation. 72
3.11 Plots of power density in frequency space as a function of density for channel widths (a) $w_{ch} = 15$ μm, (b) $w_{ch} = 25$ μm, (c) $w_{ch} = 50$ μm and (d) $w_{ch} = 75$ μm. The blue (solid) lines indicate the first five Floquet modes of the fundamental radial eigenmode, while the red (dot-dash) lines indicate the same for the second radial eigenmode, as predicted by the small δ theory. 73
3.12 Log plots of power density in frequency space as a function of density for channel widths (a) $w_{ch} = 50$ μm and (b) $w_{ch} = 75$ μm. These demonstrate that the predicted frequencies are accurate for large channel widths also. 76

A.1 Dispersion plots generated by evaluating a finite-sized version of the determinant shown in Eq. (A.1). Fig. (a) contains the dispersion construction discussed in Section 3.2, which is the dispersion relation from a single-element determinant reproduced many times. The remaining Figures contain dispersion curves calculated for (b) 3, (c) 9 and (d) 15 non-zero Fourier coefficients. 81
A.2 Frequencies of lightline intersections with the dispersion curves in Fig. A.1(a) (blue, solid) and Fig. A.1(d) (red, dots) for (a) $\delta = 0.05$ and (b) $\delta = 0.9$. Note that the blue curves correspond to the solution presented in Eq. (3.11). 82

Chapter 1

Introduction

The availability of compact short-pulse laser systems have made the interaction of short, intense laser pulses with various forms of matter a common occurrence in university-scale laboratories. This thesis is an assemblage of two publications in which we explore the effects of the passage of such a laser pulse through a molecular gas and through a density-modulated plasma channel.

In Chapter 2 the system under study is a gas of diatomic molecules in which a set of rotational revivals has been created. When a short laser pulse interacts with a gas of molecules, it excites a broad superposition of angular momentum states in the wavefunctions of each molecule. Assuming that the laser frequency doesn't match the frequencies of any of the rotational transitions, this excitation occurs through the two-photon Raman process. This results in a transient increase in the average molecular alignment, whose peak typically occurs after the pulse peak because the rotational timescale is longer than the laser pulse length. The so-called rotational revivals, in which one observes periodic molecular alignment at later times under field free conditions, occur because the energy dependence of the basis states in the wavefunction leads to their subsequent phase-realignment.

We consider the effect that the background electric field has on the amplitudes of the molecular alignment peaks. Such a background field may be produced by a

plasma that is created by the same laser pulse that sets up the rotational revivals. This affects the evolution of the off-diagonal elements of the density matrix, which evolve in both amplitude and phase. The expectation is that the revival structure will decay primarily due to the phase change, since it is phase alignment and dealignment that creates and destroys a revival peak over a very short timescale.

We perform simulations of the density matrix evolution, using the dressed particle technique to model the fluctuating electric field. We study how the amplitude of the revival peaks changes with time when the molecule interacts through a specific multipole moment. We find revival decay rates from the results of these simulations for various plasma temperatures and densities, and compare the results with decay time estimates made using a simple model to estimate the phase change in the molecular wavefunction. The estimates match the simulation results remarkably well. In addition, we compare the expected decay rate with the rate measured for revival decay due to molecular collisions, and find that they are similar for small plasma ionization fractions.

In Chapter 3 we investigate the production of THz radiation in a corrugated plasma waveguide, which consists of a plasma channel in which there are periodic axial density variations. Such a channel is created in the laboratory using a laser pulse that is line-focused onto a cluster jet with an axicon (a conical lens). To produce a corrugated plasma channel, one needs either a cluster jet with periodic density variations or a transmissive ring grating placed before the axicon to produce radial intensity modulations in the pulse.

We study the structure of electromagnetic modes in a corrugated plasma chan-

nel, and their excitation by a laser pulse. We estimate the expected frequencies of generated radiation using an analytic approach based on the assumption that the plasma density increases radially without bound, and we discuss the leakage of generated modes from the sides of a more-realistic channel in the context of WKB theory.

We discuss the details of a code written to model the response of the plasma channel to a non-evolving laser pulse. We then use this code to perform simulations of a laser pulse passing through a corrugated plasma channel that possesses realistic features, namely a maximum density at some radius, and a cutoff radius beyond which no plasma is present. We study Poynting fluxes using Fourier techniques to obtain the frequency and amount of generated radiation, and we also study field quantities in order to obtain the spatial structure of the generated modes. Finally we use a simple laser evolution model and the result of our simulations to estimate the amount of energy that can be converted to THz radiation.

This thesis is based on the following publications:

- Chapter 2: A. J. Pearson and T. M. Antonsen, *Effect of electric-field fluctuations on rotational revival amplitudes*, Phys. Rev. A. **80** 053411 (2009)

- Chapter 3: A. J. Pearson, T. M. Antonsen and J. Palastro, *Simulation of terahertz generation in corrugated plasma waveguides*, accepted for publication in Phys. Rev. E. (April 2011)

Chapter 2

The Effect of Electric Field Fluctuations on Rotational Revival Amplitudes

2.1 Introduction

There has been intense study of laser-induced molecular alignment in recent years [1, 2], because of the availability of relatively small, high-power short-pulse lasers. Here we are interested in non-resonant, non-adiabatic alignment [3, 4]. In this case, a laser pulse with a duration much less than the inverse of the frequency associated with the first excited rotational state of the molecule, and with a frequency that does not match any rotational transitions, excites a phase-coherent broad superposition of angular momentum states through a two-photon Raman process.

The result is an increase in the ensemble-averaged molecular alignment, which occurs slightly after the peak of the laser pulse because of the difference in timescales between the pulse length and the molecular rotation [5]. Because of the energy dependence of the basis states of a rigid rotor however, the phase alignment of the molecular wavefunction is periodic in time. Accordingly, the ensemble average alignment exhibits a series of sharp peaks that occur long after the laser pulse has passed [6]. These peaks are referred to as 'rotational revivals'. Experimentally, this effect can be observed by measuring the variation in the refractive index of the gas

[7], or by Coulomb explosion imaging [8].

In an ideal system, the rotational revivals would continue indefinitely, however in real systems, dissipative effects cause a loss of coherence between the phases of the various basis states [9]. If the change in phase is small on the timescale of the revivals, the amplitudes of successive alignment peaks reduce until the revival structure disappears. Conversely, if the change in phase is large, the revival structure will be absent. A major contribution to this dissipation comes from molecular collisions [10]. In this chapter we investigate an additional mechanism for the disappearance of the revival structure, involving the electric field of a background plasma and its coupling to the various multipole moments of the molecules.

The chapter is organized as follows: In Section 2.2, we consider the different parameters involved in our system, and provide some justifying remarks to establish the relevance of the effect under consideration. In Section 3.2, we discuss the use of the density matrix to model an ensemble of molecules and its evolution, the ways in which the molecules couple to electric fields and a method for modeling the fluctuating field at a point due to the presence of a background plasma. In Section 3.4 we discuss the numerical techniques used, present the results of the numerical simulations for a variety of system parameters, and compare the results to scaling laws produced by a toy model.

2.2 Decoherence due to electric field fluctuations

We begin by establishing the conditions of relevance of the proposed effect. Specifically, we wish to show that the effect is observable for a reasonable choice of plasma parameters. As previously noted, rotational revivals occur because of a periodic phase alignment of the time evolution factors in the wavefunction. Over time, decoherence occurs because of time dependent alterations of each phase factor by either collisions or, as proposed in this chapter, a fluctuating electric field. The effect of the decoherence is the decay of the rotational revivals.

In this work we quantify the alignment using the ensemble-averaged quantity $\langle \cos^2\theta \rangle$. Here, θ is the angle between the molecular axis and the polarization vector of the linearly polarized laser pulse that creates the revivals. The alignment takes the general form

$$\langle \cos^2\theta \rangle = \sum_{l=0}^{\infty} \sum_{j=0}^{\infty} c_{lj}(t) \exp\left[i(E_l - E_j)/\hbar \right] , \tag{2.1}$$

where the quantities E_l are eigenvalues of the field-free Hamiltonian and the coefficients $c_{lj}(t)$ are time-independent in field-free conditions. In this work we will consider simple linear molecules modeled as rigid rotors. The field-free Hamiltonian is therefore proportional to the total angular momentum operator $\hat{L}^2$, and its eigenstates are $|l, m\rangle$.

To estimate the revival decay time, we consider the phase change that occurs in Eq. (2.1) because of the rotational energy level shift for a molecule that interacts

with a static electric field. This energy shift is calculated using time-independent perturbation theory. For a molecule with a permanent dipole moment, the phase shift in Eq. (2.1) is proportional to

$$\Delta E_l - \Delta E_j \sim \frac{\mu^2 E_I^2}{B}\left(\frac{1}{(l+1)(l+2)-l(l+1)} - \frac{1}{(j+1)(j+2)-j(j+1)}\right), \quad (2.2)$$

where μ is the permanent dipole moment of the molecule, $B = \hbar^2/2I$ is the rotational constant and E_I is the magnitude of the electric field. This result is from second order in perturbation theory, which is necessary because of the selection rules associated with the matrix elements of the permanent dipole moment. The various factors of l and j come from the term $1/(E_l - E_j)$ that occurs in each term in the sum over states.

The decay time τ_D is given by $\tau_D \sim \hbar/(\Delta E_l - \Delta E_{l+2})$. The use of $j = l + 2$ here comes from the selection rules for an induced dipole moment. The induced dipole is the means by which a laser pulse creates a set of rotational revivals, and so it is these terms that will be present in the alignment sum before the decoherence begins.

For a numerical value of the decay time, we must choose values for the electric field E_I and for l. We choose an electric field strength of $E_I = e/r_I^2$. This is the field associated with a stationary ion at a distance corresponding to the typical molecular spacing $r_I \sim n^{-1/3}$. To choose l, we note that for a thermally distributed gas of rigid rotors, the maximally populated l state is $l_{max} \simeq \sqrt{k_B T/2B}$. For HCN at room temperature, this gives $l_{max} \simeq 8$. The resulting decay time estimate for a plasma

density of $n = 10^{18}$ cm^{-3} is $\tau_D \sim 10$ ps.

We wish to compare the decay time estimated using this method to the decay time due to collisional decoherence. We consider the measurements made by Chen et. al. [7] for N_2O at different pressures. These measurements give collisional decay times of $10-25$ ps at room temperature for pressures in the range $2-7$ atmospheres. This corresponds to gas densities of 5×10^{19} to 1.5×10^{20} cm^{-3}. The implication is that for a relatively small ionization fraction of a gas, the decay times due to a background plasma are comparable to those due to molecular collisions.

The decay time estimate made using Eq. (2.2) assumes that the ions are stationary, however we compare the result to a collisional decay time in a room temperature gas. This is permissible, since we expect the decay time due to a cold plasma to be longer than that due to a warm plasma. The reason is that in a warm plasma, decay will occur due to several ion encounters per molecule, and there is a probability that some of these will have impact parameters less than r_I, resulting in a large phase shift and thus a shorter decay time.

We expect permanent dipoles to interact much more strongly with the background field than permanent quadrupoles and induced dipoles. The energy level shift estimated in Eq. (2.2) is from second order time-independent perturbation theory, because the selection rules for a permanent dipole don't allow a first-order term. This is not the case for the permanent quadrupole and induced dipole interactions, and these have energy level shifts $\Delta E^{(Q)} \sim \Delta Q E_I / r_I$ and $\Delta E^{(I)} \sim \Delta \alpha E_I^2$ respectively. For the HCN molecule, these imply decay times several times larger for the quadrupole, and three orders of magnitude larger for the induced dipole.

We conclude from these heuristic investigations that it is quite possible to observe this effect in an appropriately designed experiment. A foreseeable difficulty is generating the rotational revivals with the desired amplitude and ionizing the gas to the desired degree, all using a single laser pulse. To alleviate this problem, one may imagine a molecular gas that is partially ionized to create a plasma of the correct density and temperature, by choosing the pulse length, intensity, gas temperature and gas mixture appropriately. If this plasma is left a sufficiently long time, then any rotational revivals generated by the first pulse will decay due to collisional decoherence and the plasma will have time to thermalize. A second laser pulse (weaker, so as not to change the state of ionization) may then be introduced, and will generate another set of coherences. The effects of the background plasma on these coherences may then be measured.

2.3 Modeling a gas of diatomic molecules

2.3.1 Density matrix formalism

Our goal in this chapter is to calculate the ensemble average alignment in a gas of diatomic molecules after the passage of a laser pulse, and to demonstrate that a fluctuating electric field results in the decay of the rotational revival amplitudes. To quantify the alignment, we choose to calculate the ensemble average of $\cos^2\theta$, where θ is the angle between the symmetry axis of a molecule and a fixed, but arbitrarily chosen, measurement axis.

To model a molecule, we note that for molecules at room temperature, the

energy of the first excited vibrational level and the first excited electronic level are small compared to the thermal energy. For example, an N_2 molecule has vibrational energies in spectroscopic units of order 10^3 cm^{-1} and electronic energies of order 10^5 cm^{-1}. For comparison, the rotational energy of ground state hydrogen is 2 cm^{-1} and the thermal energy in a gas at 300 Kelvin is approximately 200 cm^{-1}. We conclude that it is appropriate to restrict our attention to rotational excitations.

Given the above considerations, we model the molecule as a rigid rotor, which has energy levels

$$E_l = Bl(l+1) - Dl^2(l+1)^2\,, \tag{2.3}$$

where l is the total angular momentum quantum number, $B = \hbar^2/2I$ is the rotational constant and D is the energy modification due to centrifugal stretching.

In the density matrix formalism, the ensemble average alignment is given by

$$\langle \cos^2\theta \rangle = \mathrm{Tr}(\hat{\rho}\cos^2\theta) = \sum_{l=0}^{\infty}\sum_{m=-l}^{l}\sum_{j=0}^{\infty}\sum_{n=-j}^{j}\rho_{lmjn}\langle jn|\cos^2\theta|lm\rangle\,, \tag{2.4}$$

where $\hat{\rho}$ is the density operator. On the right hand side of Eq. 2.4, we have written the trace using the eigenstates of the Hamiltonian $\hat{H}_0 = (B/\hbar^2)\hat{L}^2$. These are the standard angular momentum eigenkets that satisfy $\langle\theta\phi|lm\rangle = Y_{lm}(\theta,\phi)$. Note that that in Eq. 2.3 $D \ll B$, and so while the centrifugal distortion constitutes an $\mathcal{O}(D/B)$ correction to the eigenvalues of $\hat{H}_0$, the eigenstates remain unaffected.

Continuing in the $|lm\rangle$ basis, the evolution of the density matrix is governed

by

$$\frac{d}{dt}\rho_{lmjn} = -i\omega_{lj}\rho_{lmjn} + \frac{i}{\hbar}\sum_{k=0}^{\infty}\sum_{o=-k}^{k}\left(\rho_{lmko}V_{kojn} - V_{lmko}\rho_{kojn}\right), \tag{2.5}$$

where V_{lmjn} is an interaction matrix element and $\omega_{lj} = (E_l - E_j)/\hbar$. The interaction matrices we consider take the form

$$V_{lmjn} = -\langle lm|\hat{\boldsymbol{\mu}} \cdot \boldsymbol{E}|jn\rangle \tag{2.6}$$

$$V_{lmjn} = -\frac{1}{2}\langle lm|\boldsymbol{E} \cdot \underline{\hat{\boldsymbol{\alpha}}} \cdot \boldsymbol{E}|jn\rangle \tag{2.7}$$

$$V_{lmjn} = -\frac{1}{6}\langle lm|\underline{\hat{\boldsymbol{Q}}} : \boldsymbol{\nabla}\boldsymbol{E}|jn\rangle \tag{2.8}$$

where $\hat{\boldsymbol{\mu}}$ is the permanent dipole moment operator, $\underline{\hat{\boldsymbol{\alpha}}}$ is the polarizability operator, $\underline{\hat{\boldsymbol{Q}}}$ is the (traceless) permanent quadrupole moment operator and $\boldsymbol{E}$ is the electric field vector.

2.3.2 Molecular alignment by a linearly polarized laser pulse

Here we consider two qualitatively distinct electric fields. The first is the electric field of a short laser pulse, which is used to create a rotational revival structure in a molecular gas. We are interested in pulse lengths that are long compared to the optical period, but short compared to the typical rotational timescale of a small diatomic molecule (on the order of picoseconds), and laser frequencies that are large compared to the inverse rotational timescale. This places us in the regime of non-adiabatic, non-resonant molecular alignment. Assuming there are many cycles over the duration of the pulse, we cycle-average the interaction matrices. A consequence

of this is that interaction terms with odd powers in the field strength are negligible compared to those with even powers. We conclude that only the induced dipole term is relevant for the laser pulse.

In the body-fixed frame of a molecule with the molecular axis chosen as the z-axis, the polarizability tensor may be written as a diagonal matrix with entries α_{xx}, α_{yy} and α_{zz}. In a coordinate system in which the molecular axis is defined by a unit vector $\hat{\boldsymbol{n}}$, the polarizability tensor takes the form

$$\underline{\boldsymbol{\alpha}} = \alpha_\perp \underline{\mathbf{1}} + \Delta\alpha \hat{\boldsymbol{n}}\hat{\boldsymbol{n}}\,, \tag{2.9}$$

where $\alpha_\perp = \alpha_{xx} = \alpha_{yy}$ and $\Delta\alpha = \alpha_{zz} - \alpha_\perp$.

Assuming that the laser pulse is linearly polarized, we choose the polarization vector, the z-axis of our coordinate system, and the measurement axis for the angular momentum to coincide. The laser field is written as

$$\boldsymbol{E}(t) = \mathrm{Re}\{\hat{\boldsymbol{z}} E_0(t) \exp(-i\omega t)\}\,. \tag{2.10}$$

Substituting this into Eq. (2.7) and cycle averaging, we obtain

$$V^{(\mathrm{L})}_{lmjn} = -\frac{1}{4} E_0^2(t) \Big(\alpha_\perp \delta_{lj}\delta_{mn} + \Delta\alpha \langle lm| \cos^2\theta |jn\rangle \Big)\,, \tag{2.11}$$

where we have used $\hat{\boldsymbol{n}} \cdot \hat{\boldsymbol{z}} = \cos\theta$. The second term in Eq. (2.11) may be calculated by conversion to an integral over a solid angle of a product of spherical harmonics. We note that the density matrix elements do not depend on $\alpha_\perp$, since the total

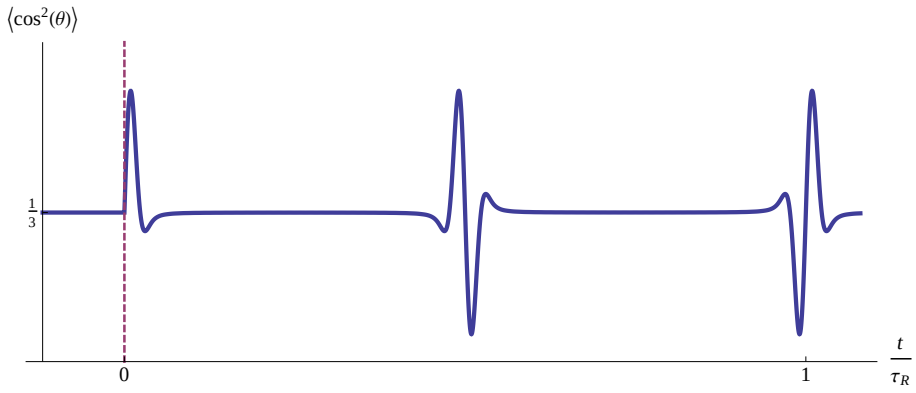

Figure 2.1: Ensemble average alignment vs. time calculated in the zero-pulse-length limit. Plot domain includes the laser pulse at $t = 0$ and the first full revival at $t = \tau_R$. Note that the first peak of the alignment occurs after the laser pulse, due to the characteristic response time of the molecules. This feature is preserved in short, finite-length pulses.

contribution to the density matrix evolution equation (Eq. (2.5)) from the first term in Eq. (2.11) vanishes identically.

The evolution of the density matrix elements for the molecule subjected to a laser pulse may now be found using either perturbation theory, the zero-pulse-length limit ($E_0^2(t) \sim \delta(t - t_0)$), or numerical techniques. For the zero pulse length limit, one revival period of the ensemble average alignment is displayed in Fig. 2.1.

2.3.3 Interaction matrix for a fluctuating background electric field

The other type of electric field considered is the fluctuating background field due to the presence of a plasma. Unlike the case of a linearly polarized laser pulse, we cannot choose to align the electric field vector and the angular momentum measurement axis. Thus, the angular dependence of the interaction terms are of greater complexity. Keeping the z-axis as the angular momentum measurement axis, we

define the function

$$W = \hat{\boldsymbol{n}} \cdot \boldsymbol{E} = E_x \sin\theta\cos\phi + E_y \sin\theta\sin\phi + E_z \cos\theta\,. \tag{2.12}$$

The interaction terms for each type of coupling are given by

$$V^{(\mathrm{P})}_{lmjn} = -\,|\boldsymbol{\mu}|\langle lm|W|jn\rangle \tag{2.13}$$

$$V^{(\mathrm{Q})}_{lmjn} = -\,\frac{1}{6}\Big(Q_\perp \boldsymbol{\nabla}\cdot\boldsymbol{E}\delta_{lj}\delta_{mn} + \Delta Q\langle lm|\hat{\boldsymbol{n}}\cdot\boldsymbol{\nabla}W|jn\rangle\Big) \tag{2.14}$$

$$V^{(\mathrm{I})}_{lmjn} = -\,\frac{1}{2}\Big(\alpha_\perp|\boldsymbol{E}|^2\delta_{lj}\delta_{mn} + \Delta\alpha\langle lm|W^2|jn\rangle\Big)\,, \tag{2.15}$$

where we have written the quadrupole tensor elements in analogy to Eq. (2.9). Note that the quadrupole coefficients are related because of the traceless nature of the quadrupole tensor. By convention, we have $Q_\perp = -\frac{1}{2}Q_{zz}$ and $\Delta Q = \frac{3}{2}Q_{zz}$ where z is the symmetry axis of the molecule. Note also that as in Eq (2.11), the $Q_\perp$ and $\alpha_\perp$ terms will not contribute to the density matrix evolution.

We wish to study the effect of a fluctuating background field on the revival structure created by the laser pulse. In general, this problem cannot be solved analytically, and so we resort to a numerical solution. We proceed by modeling the plasma as a collection of dressed particles [11]. In this method, we consider a test particle moving in a straight line through a plasma at some velocity $\boldsymbol{v}$. Such a particle will acquire a shielding cloud from the plasma, and this will alter its potential. For a test particle at rest, this is the familiar Debye shielding effect, but for a moving particle the shielding is modified in an anisotropic way. We refer to

the combination of the test particle and its shielding cloud as a dressed particle.

Following the formulation of Krall and Trivelpiece [12], we calculate the potential for a dressed particle by solving the coupled Poisson and linearized Vlasov equations. By doing so we assume that the dressed particle is non-relativistic and moving at uniform velocity, and that the plasma is only slightly perturbed by its presence. The solution proceeds by Fourier-transforming in space and Laplace-transforming in time. The time-asymptotic solution neglects both transients from the initial perturbation and excited normal modes of the plasma that vanish due to Landau damping, and is given by

$$\phi(\boldsymbol{x}_{ob}, \boldsymbol{x}, \boldsymbol{v}, t) = 4\pi q \int \frac{d^3k}{(2\pi)^3} \frac{\exp\left(i\boldsymbol{k} \cdot (\boldsymbol{x}_{ob} - \boldsymbol{x} - \boldsymbol{v}t)\right)}{k^2 D(\boldsymbol{k}, \boldsymbol{k} \cdot \boldsymbol{v})}\,, \tag{2.16}$$

where $\boldsymbol{x}$ is the initial position of the dressed particle $\boldsymbol{x}_{ob}$ is the point of observation of the potential . $D(\boldsymbol{k}, \boldsymbol{k} \cdot \boldsymbol{v})$ is the dielectric function of the plasma, given by

$$D(\boldsymbol{k}, \boldsymbol{k} \cdot \boldsymbol{v}) = 1 - \sum_{\alpha} \frac{\omega_{p\alpha}^2}{k^2} \int \frac{d^3v'}{(2\pi)^3} \frac{\boldsymbol{k} \cdot \boldsymbol{\nabla}_{\boldsymbol{v}'} f_{0\alpha}}{\boldsymbol{k} \cdot (\boldsymbol{v}' - \boldsymbol{v}) - i0^+}\,, \tag{2.17}$$

where α refers to the plasma species and $f_{0\alpha}$ is the unperturbed plasma distribution function.

We note that in the current approach we take the test particle velocities to be constant and unaffected by the molecule's electric field. The result is that over time there will be continuous energy transfer from the plasma particles to the molecule. In reality, the energy gain of the molecule is limited, and the molecule will come

into thermal equilibrium with the plasma. We assume that this process occurs over a longer period of time than the destruction of the recurrences.

The plasma will be created by the partial ionization of the molecular gas by the laser pulse. Since this is very short, we expect the molecular ions to be thermally distributed at the same temperature as the unionized molecules. The electrons will in general be much faster than the ions. We therefore use a dressed particle model with molecule-mass test particles, shielded by fast electrons and stationary ions. We choose to exclude electrons as test particles because we expect the ions to remain in proximity to a molecule for much longer than the electrons, and so the ions will have the dominant effect. In this case, we are interested in the low speed approximation for the potential. This calculation may be found in Ref. [13], and the result is

$$\phi(\boldsymbol{r},\boldsymbol{v}) \simeq \frac{q}{r}\left(\exp\left(-rk_D\right) + \frac{v}{u_{th}} g(r, \hat{\boldsymbol{r}}\cdot\hat{\boldsymbol{v}}) + \cdots \right), \tag{2.18}$$

where $\boldsymbol{r} = \boldsymbol{x}_{ob} - \boldsymbol{x} - \boldsymbol{v}t$, $\boldsymbol{v}$ is the test particle velocity, u_{th} is the electron thermal velocity, and k_D is the Debye wavenumber. The function $g(r, \boldsymbol{r}\cdot\boldsymbol{v})$ is given by

$$\begin{aligned} g(r,\hat{\boldsymbol{r}}\cdot\hat{\boldsymbol{v}}) = \frac{1}{\sqrt{2\pi}}(\hat{\boldsymbol{r}}\cdot\hat{\boldsymbol{v}})\Bigg[&\frac{rk_D}{2}\left(1 - \frac{1}{rk_D} + \frac{1}{(rk_D)^2}\right)\exp\left(rk_D\right)E_1(rk_D) \\ &+ \frac{rk_D}{2}\left(1 + \frac{1}{rk_D} + \frac{1}{(rk_D)^2}\right)\exp\left(-rk_D\right)\mathrm{Ei}(rk_D) - 1\Bigg], \end{aligned} \tag{2.19}$$

where E_1 and Ei are exponential integral functions.

Once we calculate the electric field for a collection of test particles, we may compute the density matrix and thus the ensemble average molecular alignment over

the various rotational states available, as per Eq. (2.4). We then repeat this procedure for a number of different test particle configurations to generate an ensemble average of the molecular alignment.

2.4 Numerical Simulation Results

In this section we present the results of the numerical simulations. As previously stated, the goal is to calculate the time-dependent expectation value $\langle \cos^2 \theta \rangle$ for a fluctuating background field. We simulate the background field by calculating the electric field components at the center of a spherical region containing a number of test particles. These test particles move in straight lines from random initial positions and with random velocities, all generated from the appropriate distribution functions. Test particles that leave this region are replaced by re-generating their initial conditions to place them somewhere on the system boundary with an ingoing velocity. The number of test particles present in the system at any one time is chosen to correspond to a certain plasma density.

To calculate the density matrix elements, we use the Cash-Karp embedded Runge-Kutta method [14]. This allows for an efficient adaptive stepsize calculation. We begin with a thermal distribution of rotational states, and calculate the effect of the laser pulse strike on the density matrix. We will consider a laser pulse with an intensity of 10^{12} W/cm^2, which is large enough to create a revival structure while avoiding complications introduced when the populations of the angular momentum states change significantly. This intensity is not sufficient to cause the appropriate

level of ionization, and so our simulations correspond to an experiment of the type described in the last paragraph of Section 2.2. We choose the pulse length to be 100 fs and the optical frequency to be 10^{15} Hz, both typical of a short-pulse laser. This optical frequency will be sufficiently large compared to the characteristic molecule rotational frequency as to allow the cycle averaging discussed in the derivation of Eq. (2.11).

The density matrix calculated for the laser pulse is then used as an initial condition for the calculation of the evolution of the density matrix with the fluctuating background field present. We use this result to calculate the amount of alignment of a single molecule in the gas, and then repeat this procedure for a large number of test particle configurations, so as to obtain an average over many molecules.

In these simulations, we will consider the molecules Hydrogen Cyanide (HCN) and Nitrogen (N_2). HCN is an example of a linear molecule with a strong permanent dipole moment, while N_2 is a common dipole. We will consider the different multipole interactions separately, since we expect their sizes to differ significantly from one another. This may be seen by estimating in each case the size of the interaction term for a Coulomb field at distance $n^{-1/3}$. The free parameters in these simulations are the electron and ion temperatures, and the plasma density.

The first set of results are for HCN with the background ions at room temperature. The parameters for HCN associated with the molecular dynamics are $B = 1.48$ cm^{-1} and $D = 3.33 \times 10^{-6}$ cm^{-1}, and multipole moments are $|\boldsymbol{\mu}| = 2.96 \times 10^{-18}$ esu cm [15], $\Delta Q = 7.68 \times 10^{-26}$ esu cm^2 and $\Delta\alpha = 2.0 \times 10^{-24}$ cm^3 [16]. We considered electron temperatures of 1 and 10 eV, and for the permanent dipole case, we chose a

plasma density of 10^{18} cm^{-3}. For higher order moments, we chose higher densities, since we expect the decay time to be longer. This choice reduces computation time and avoids large-time effects associated the the centrifugal stretching.

Fig. 2.2 demonstrates the revival structure and the decay. In Figures 2.2(a) and 2.2(b) only the permanent dipole interaction is allowed, in Fig. 2.2(c) only the permanent quadrupole interaction is allowed, and in 2.2(d) only the induced dipole interaction is allowed. As the permanent dipole interaction is strongest, followed by the quadrupole and induced dipole interaction, similar decay times occur at lower densities in Figures 2.2(a) and 2.2(b). To understand the revival structure, we consider the form of the average alignment, as seen in Eq. (2.4). This may be rewritten

$$\langle \cos^2\theta \rangle = \sum_{l=0}^{\infty} \sum_{m=-l}^{l} \sum_{j=0}^{\infty} \sum_{n=-j}^{j} \alpha_{lmjn} \langle jn| \cos^2\theta |lm\rangle \exp\left(-i\omega_{lj}t\right), \tag{2.20}$$

where $\alpha_{lmjn} = \rho_{lmjn} \exp\left(i\omega_{lj}t\right)$. This was seen originally in Eq. (2.1). In field-free conditions α_{lmjn} is a constant, and revival peaks occur because the phase factors in Eq. (2.20) align periodically. Comparing Eq. (2.3) and (2.20), the revival period is seen to be $\tau = \pi\hbar/B$. For HCN, the revival period is calculated to be $\tau = 11.3$ ps, which is consistent with our results. At the halfway point between revival peaks, there exist sharp decreases in the alignment. This is because at half revival times, half of the complex exponentials in Eq. (2.20) are phase aligned with value 1 and the other half are aligned with value -1. The terms in the sum thus interfere destructively leading to a decrease in the alignment.

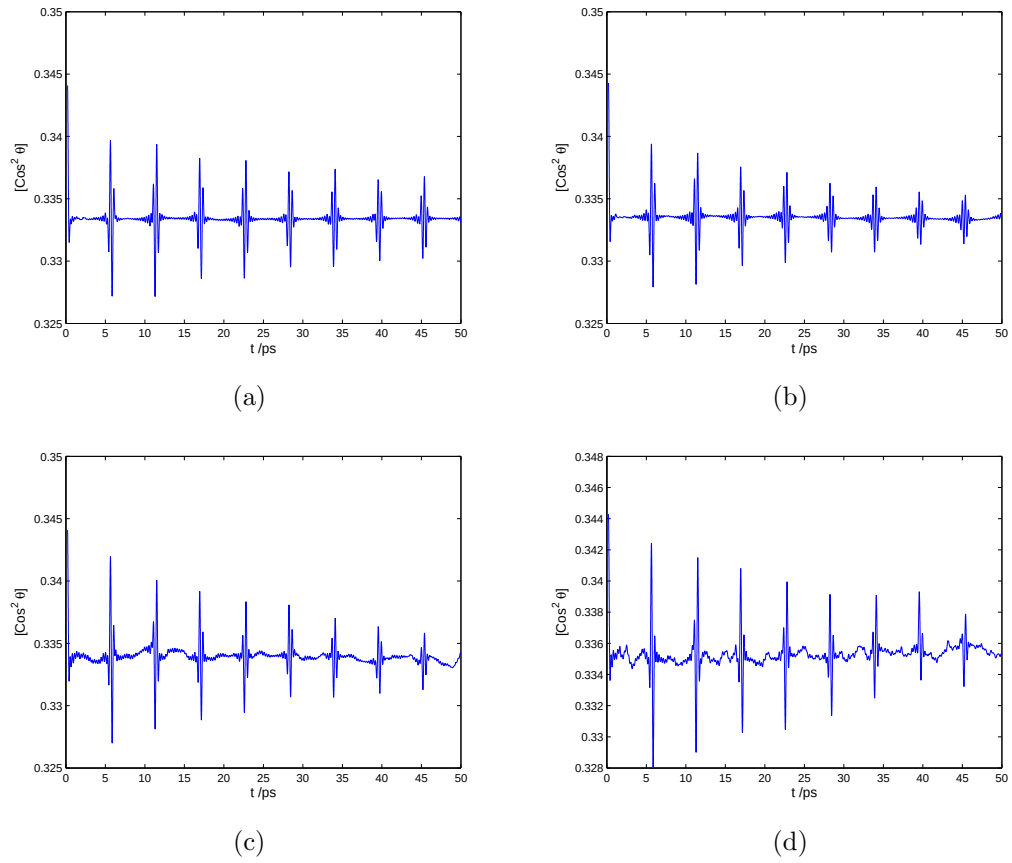

Figure 2.2: Ensemble-averaged alignment as a function of time for HCN molecules in a plasma with room temperature ions. In (a) the interaction considered is the permanent dipole, the plasma density is $n = 10^{18}$ cm^{-3} and the electron temperature is T$_e$ =1 eV. In (b), the electron temperature has been increased to T$_e$ =10 eV. In (c) the interaction considered is the permanent quadrupole, the plasma density has increased $n = 10^{19}$ cm^{-3} and the electron temperature is once again T$_e$ =1 eV, while in (d) the interaction considered is the induced dipole, the plasma density is $n = 10^{20}$ cm^{-3} and the electron temperature is T$_e$ =1 eV.

There is a second set of peaks due to the second term in Eq. (2.3). Because the constant D is much smaller than B however, these peaks are much wider than the revival peaks, and their recurrence period is much larger. If we were to observe a revival structure in the absence of decoherence for a sufficiently long time, we would observe the revival peaks reducing in size until they vanish, and then periodically reappear at times $\tau_D = \pi\hbar/D$. We tend not to observe this effect since regardless of mechanism, there is always sufficient decoherence to destroy the revival structure before time τ_D.

In the presence of a background plasma, the coefficients α_{lmjn} are no longer constant, but are time dependent complex functions. For each set of test particles, the complex exponential part of each term in the sum in Eq. (2.20) is modified by the phase of the coefficient. If the phase change in the coefficient is small between the laser strike and the first revival time, then the amplitude of each revival peak is reduced. At later times, the phase change is greater than at earlier times, and so the amplitude reduction is also larger. Eventually, the revival peaks are destroyed completely. If the phase change becomes large on a timescale smaller than the recurrence time, then the revival structure is destroyed before the first peak appears.

The next set of results is for N_2, again with the ions at room temperature. The molecular parameters for N_2 are $B = 1.99$ cm^{-1} and $D = 5.76 \times 10^{-6}$ cm^{-1} [17]. The quadrupole moment for N_2 is $\Delta Q = 1.49 \times 10^{-26}$ esu cm^2, and the induced dipole moment is $\Delta\alpha = 9.3 \times 10^{-25}$ cm^3 [16]. As before, the density for the quadrupole case is $n = 10^{19}$ cm^{-3} and for the induced dipole case is $n = 10^{20}$ cm^{-3}.

The graphs in Fig. 2.3 once more demonstrate the revival structure. We note

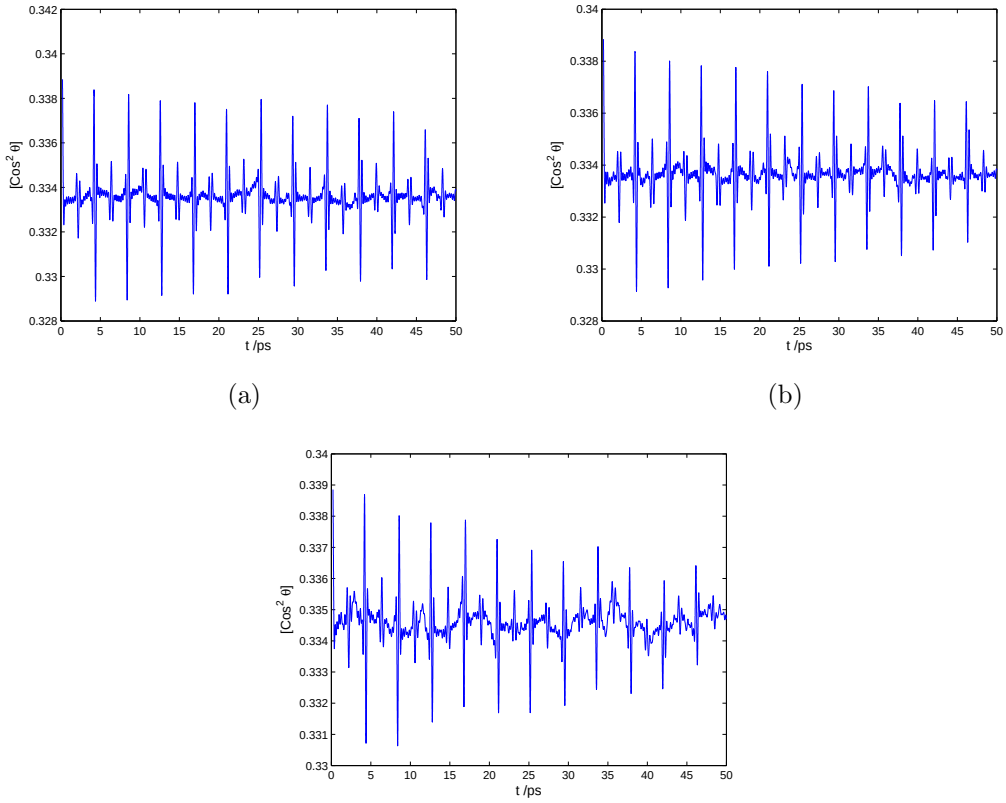

Figure 2.3: Ensemble-averaged alignment as a function of time for N_2 molecules in a plasma with room temperature ions. In (a) the interaction considered is the permanent quadrupole, the plasma density is $n = 10^{19}$ cm^{-3} and the electron temperature is T_e =1 eV. In (b), the electron temperature has been increased to T_e =10 eV. In (c) the interaction considered is the induced dipole, the plasma density has increased $n = 10^{20}$ cm^{-3} and the electron temperature is once again T_e =1 eV.

that the decay time is much greater for N_2 than for HCN (in the case where only the quadrupole moment of HCN is considered). This is because the quadrupole coupling constant for HCN is $\sim$5 times greater than that for N_2, and so the background field is much more effective in exciting different rotational states of the molecules and disrupting the phase coherence of the revivals. In the N_2 graph, the additional peaks at $\tau/4$ and $3\tau/4$ are due to the requirement that the wavefunction of N_2 must be symmetric under exchange of the nuclei, since Nitrogen atoms are spin-1 bosons. This means, for example, that if the rotational part of the wavefunction for the molecule is even, then only even two-nucleus wavefunctions are allowed, thus creating a symmetric total wavefunction. For combinations of two spin-1 particles there are 6 symmetric states and 3 antisymmetric states. Thus, the populations of even rotational states are weighted by a factor of two, and the sum of all the phase factors in Eq. (2.20) no longer cancel exactly at the quarter and three-quarter points.

The final set of results consist of a detailed study of the decay time as a function of the ion thermal velocity and the plasma density. These results are obtained by generating alignment vs. time graphs and fitting an exponential curve to the recurrence peaks. In Fig. 2.4(a), the decay times were obtained for a plasma density of 10^{18} cm^{-3}, while in Fig. 2.4(b), the results were obtained for ions with a thermal velocity corresponding to room temperature. While we varied the ion temperature in Fig. 2.4(a), the temperature associated with the distribution of angular momentum state population was fixed at room temperature. In both cases, we considered only the permanent dipole interaction for HCN, and the electron temperature was held

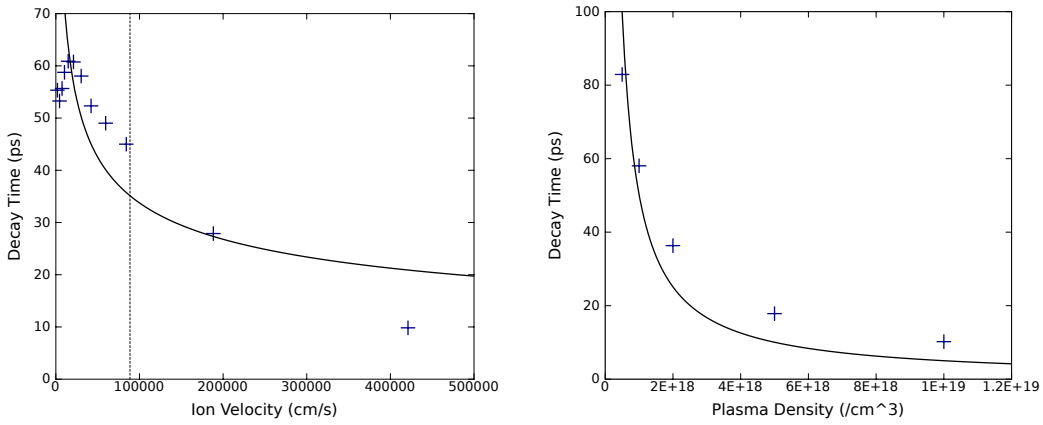

(a) (b)

Figure 2.4: Variation of decay time with system parameters. In (a), we show the decay time as a function of ion velocity, with fixed density $n = 10^{18}$ cm^{-3}. The temperature associated with the angular momentum population distribution was fixed at 300 K. In (b), we show the decay time as a function of density, with room temperature ions. In both cases, the electron temperature is fixed at 10 eV.

constant at 1 eV.

To explain these results, we consider the quantum mechanical description of a single molecule subject to the electric field of a passing ion. To begin, we note that for a constant electric field, the energy of the state $|l, m\rangle$ shifts by an amount

$$\Delta E^{(2)}_{lm} = \sum_{|jn\rangle \neq |lm\rangle} \frac{|\langle lm|\boldsymbol{\mu}\cdot\boldsymbol{E}|jn\rangle|^2}{E_l - E_j} \sim \frac{\mu^2 E_I^2}{2B}\Delta_{lm} \ , \tag{2.21}$$

c.f. Eq. (2.2). This term comes from second order time-independent perturbation theory. The first order term is $\Delta E^{(1)}_{lm} = \langle lm|\boldsymbol{\mu}\cdot\boldsymbol{E}|lm\rangle$, which vanishes.

Decoherence will occur even if all ions are stationary due to the fact that each molecule experiences a different electric field depending on its proximity to neighboring ions. The typical electric field strength a molecule experiences is $E_I \simeq e/r_I^2$, where $r_I = n^{-1/3}$ is the inter-ion spacing. The fluctuations in the electric field

strength are comparable to this value. Thus, there will be variations in ΔE_{lm}.

The functional form of the decay in time is determined by the distribution of electric field values, and is probably not exponential. Since the fluctuations in electric field magnitude are as large as the typical value we estimate that decoherence will occur in a time

$$\tau_s \sim \frac{\pi\hbar}{\Delta E_{lm} - \Delta E_{l+2m}} = \frac{2\pi\hbar B r_I^4}{\mu^2 e^2} \frac{1}{\Delta_{lm} - \Delta_{l+2m}} \sim n^{-4/3} \; . \tag{2.22}$$

Previously we posited that the phase shift that leads to decoherence was given by differences in the second order energy shift between l and $l+2$, and we have done so here also. This is motivated by the selection rules associated with the induced dipole coupling between the laser pulse and a molecule. For a sufficiently weak pulse, the non-zero off diagonal density matrix elements will have $l - j = 2$.

In Section 2.2 we ignored the angular dependence of Eq. (2.21) and chose l by finding the maximally populated state for a given temperature. This led to an estimate of $\tau \sim 10$ ps. Now we attempt to improve the decay time estimate by averaging over all possible electric field angles (relative to the angular momentum measurement axis), and by performing a weighted average over angular momentum state populations. This yields a decay time estimate of $\tau \sim 62$ ps, which is in good agreement with Fig. 2.4(a).

If the ions are moving the decoherence time can be shorter than τ. This is because with time an ion is likely to come much closer to a molecule than the typical ion spacing r_I. The strong electric field occurring during such an encounter gives

a phase change much bigger than calculated for static ions. For this regime to be of interest, the static decoherence time must be much longer than the typical time it takes an ion to move a distance equal to the inter-ion spacing, i.e. $\tau >> r_I/v_{th}$, where v_{th} is the typical ion velocity.

For the case of ions moving at a low speed such that their transit time (i.e. time spent in proximity to molecule) is large compared to the characteristic evolution time of the eigenstates, we may use the adiabatic approximation to estimate the phase change. Which states satisfy the adiabatic approximation will be discussed subsequently. For the moment we assume that all do. Here, we assume that the ion moves in a straight line with velocity v and impact parameter b and causes a time dependent energy shift

$$\Delta E \simeq \frac{\mu^2 e^2}{B} \frac{1}{(b^2 + v^2 t^2)^2} \ . \tag{2.23}$$

The total phase shift in the molecular wavefunction caused by a single ion is then

$$\Delta\phi = \int dt \frac{\Delta E(t)}{\hbar} = \frac{\pi \mu^2 e^2}{2\hbar B} \frac{1}{b^3 v} \ . \tag{2.24}$$

If we now suppose that each phase shift happens instantaneously (which is equivalent to assuming that the decay time we will calculate is long compared to the ion transit time), and further assume that the phase shifts due to different ions are independent events, we can evaluate the rate of decoherence.

To do this, we break time into N intervals of duration $\Delta t = t/N$. We assume that during each time interval, there is a probability of a random phase change $\Delta\phi$

due to a close encounter with an ion. The net phase change to the wavefunction is the sum of all random phase changes. The average of the wavefunctions of an ensemble of molecules will evolve in time according to

$$\langle \exp(i\textstyle\sum_{\Delta t}\Delta\phi)\rangle = \left(\int dP \exp(i\Delta\phi)\right)^N , \tag{2.25}$$

where dP is the probability of a phase change $\Delta\phi$ in the interval $d(\Delta\phi)$, and we have assumed that the phase changes in the N different time intervals are independent. As time $t = N\Delta t$ goes to infinity the average phase factor will decay.

We evaluate this decay by assuming that the amount of decay in a single time interval is small. Thus, we write in the $N \to \infty$ limit

$$\langle \exp(i\textstyle\sum_{\Delta t}\Delta\phi)\rangle = \left(1 + \frac{t}{N}\int \frac{dP}{\Delta t}\big(\exp(i\Delta\phi) - 1\big)\right)^N \simeq \exp\left(-\nu t\right) , \tag{2.26}$$

where

$$\nu = -\int \frac{dP}{\Delta t}\big(\exp(i\Delta\phi) - 1\big) . \tag{2.27}$$

We note the ν has both a real an an imaginary part. To evaluate the probability per unit time that there will be a phase change $\Delta\phi$ we note that in the time interval Δt the number of ions with speed v in the range dv entering a sphere of radius b surrounding the molecule is

$$dN = 4\pi b^2 n \frac{1}{\sqrt{2}v_{th}} \exp\left(-v^2/v_{th}^2\right) v dv \Delta t . \tag{2.28}$$

All of these ions will have an impact parameter less than b. Thus, the number of ions with impact parameter b in the interval db passing per unit time is obtained by differentiating with respect to b:

$$\frac{dP}{\Delta t} = \frac{dN}{db}\frac{db}{\Delta t} = \frac{8\pi^{1/2}n}{v_{th}} v \exp\left(-v^2/v_{th}^2\right) dv b db \; . \tag{2.29}$$

We may now substitute Eq. (2.24) for $\Delta\phi$, and change variables of integration to $\xi = v/v_{th}$ and $b = b_c\beta$, where

$$b_c^3 = \frac{\pi\mu^2 e^2}{2\hbar B v} \; , \tag{2.30}$$

to obtain for the decoherence time

$$\tau_d^{-1} = \nu = -n v_{th}^{1/3} \left(\frac{\pi\mu^2 e^2}{2\hbar B}\right)^{2/3} \Lambda \; , \tag{2.31}$$

where

$$\Lambda = 8\pi^{1/2} \int_0^\infty d\xi \xi^{1/3} \exp\left(-\xi^2\right) \int_0^\infty \beta d\beta \big(\exp\left(i/\beta^3\right) - 1 \big) \; . \tag{2.32}$$

Numerical evaluation gives $\Lambda = -6.43 + 11.14i$. Comparing the static decoherence time τ_s given by Eq. (2.22) and the dynamic decoherence time τ_d given by Eq. (2.31), we note that $\tau_d^{-1} \sim \tau_s^{-2/3}(v_{th}/r_I)^{1/3}$. Since at the boundary separating the static and dynamic cases $v_{th} \sim r_I/\tau_s$, the two results are in agreement.

There is some evidence of the density and temperature dependences implied by Eq. (2.31) in Fig. 2.4. Fig. 2.4(a) shows the dependence of the decoherence time on ion thermal velocity at fixed density. As the thermal velocity tends to zero the

decoherence time tends to a fixed value, which is similar to our estimated static decay time of $\tau_s = 62$ ps. As the thermal velocity is increased the decoherence time decreases. The solid line in Fig. 2.4(a) shows the estimated decay time τ_d calculated using τ_s and Eq. (2.31).

The vertical dashed line indicates the velocity of an ion with a transit time corresponding to the period of the $l = 1$ eigenstate. For larger ion velocities, we expect the adiabatic approximation to fail for $l = 1$. For large values of angular momentum quantum number however, a failure point will occur at a correspondingly larger ion velocity. For $l = 8$, the adiabatic approximation holds over the entire ion velocity range considered.

We expect the adiabatic result to apply for the density dependence of the decay time, as shown in Fig. 2.4(b). This is because the $l = 1$ adiabatic boundary remains above the ion thermal velocity for all densities considered. The solid line indicates the calculated decay time τ_d found from combining the room temperature result in Fig. 2.4(a) and the n^{-1} scaling law.

2.5 Conclusion

To summarize, we studied the effect of a fluctuating electric field on the coherence of a set of rotational revivals in a molecular gas. We do so by simulating the interaction of a molecular gas with a laser pulse, and then with a set of charged test particles. We have found that the amplitudes of the revival peaks do indeed decrease with time. The reasons for this is that the background field generated by

the test particles, through the multipole moments of the molecule, generate changes in the coherent superpositions in the molecular wavefunction. Equivalently, this changes the off-diagonal elements of the density matrix.

We compare the results of our simulations to analytic estimates of the decay time. To make these estimates, we assume that the phase changes in the off-diagonal elements are of far greater importance in causing decoherence than the amplitude changes, since almost-perfect phase alignment is required to generate a revival peak, which is a very narrow structure in time. Using the adiabatic approximation and time-independent perturbation theory, we estimate the typical phase change that occurs as a function of ion temperature and density. From this, we estimate the revival decay time and compare it to decay times extracted from the simulations. The results are surprisingly good, given the complexities of the decoherence process and the simplicity of our model.

Both the numerical and analytic results follow the expect trends. These include decreased decay time with increasing plasma density and increasing ion velocity, and increased decay time with higher-order multipole interactions. We found that for plasma densities of around 10^{18} cm^{-3} and ion temperatures of around room temperature, the decay time is of the order of a few tens of picoseconds. This makes the decay process discussed in this work comparable in effectiveness to collision-induced decoherence in gases with densities one-to-two orders of magnitude greater. This implies that for molecules with a sufficiently large permanent dipole moment, this effect may be observed in systems with relatively small ionization fractions.

Chapter 3

Simulation of THz Generation in Corrugated Plasma Waveguides

3.1 Introduction

Terahertz radiation lies between microwaves and infra-red in the frequency spectrum. The wide variety of possible applications utilizing THz radiation, from spectroscopy and biological imaging to national security, medicine and industry, make the development of small scale THz devices critical. Today there exists a variety of THz sources, many of which are available commercially. Small scale sources include far-infrared [18] and quantum cascade lasers [19], laser driven THz antennae [20, 21] and crystals [22], and backwards wave oscillators [23]. In general, bright THz sources are based on free electron devices, for example gyrotrons [24] and free-electron lasers [25, 26, 27]. These can be large and relatively expensive to operate, and research into new THz sources continues [28].

THz radiation generation by laser pulses in plasmas was first demonstrated by Hamster et. al. [29]. The source of this radiation is the current driven by the ponderomotive force of a laser pulse or electron beam. In order for this current to couple to one or more electromagnetic modes of the plasma, the plasma density must be inhomogeneous, or there must be a strong background magnetic field [30]. The transfer of energy from a driver to THz radiation is limited by the fact that EM modes in a plasma couple poorly to pulse-driven currents and in general have

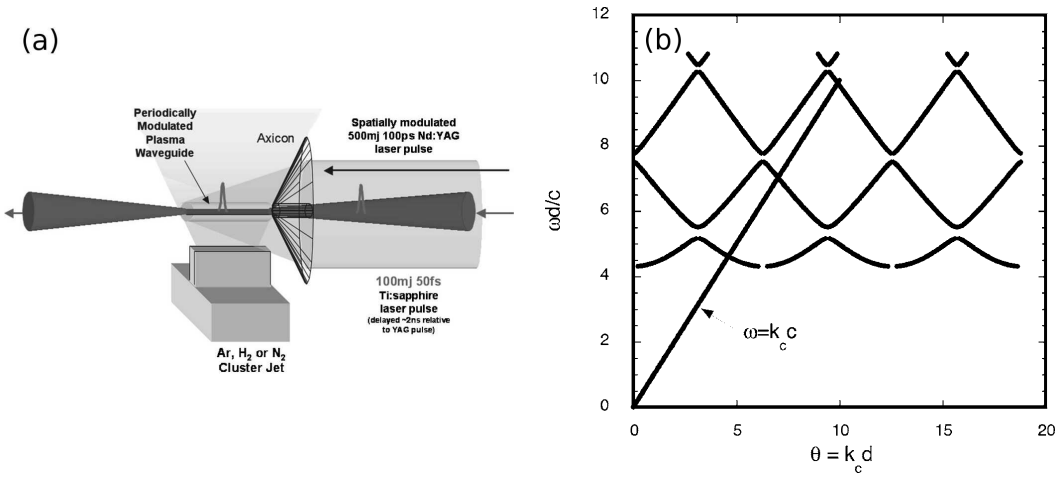

Figure 3.1: (a) Diagram of experimental setup for producing a corrugated plasma channel. As an alternative to a spatially modulated formation pulse, a modulated cluster density may be used in conjunction with a uniform formation pulse. (b) Dispersion plot of EM modes in the delta function corrugated channel (considered by Antonsen et. al.) which consists of a channel with a density profile that has a train of delta functions, thus creating a period system while allowing the use of analytic results from the axially uniform case. Here, d is the distance between consecutive delta functions, while ω and k_c are the frequency and wavenumber.

superluminal phase velocities. These modes will quickly fall out of phase with the generated current, which travels with the driver at its group velocity. THz generation has also been demonstrated by Leemans et. al. [31] in the form of transition radiation from electrons exiting a laser wakefield accelerator stage.

In this chapter we report the results of simulations that model the generation of THz radiation in corrugated plasma channels. Corrugated plasma channels are plasma channels that possess an axially periodic density profile. These channels may be produced reliably in the laboratory [32] by line-focusing a laser pulse onto a cluster jet, as shown in Fig. 3.1(a). The periodic density structure is produced by either axial modulation of the cluster density or radial modulation of the laser intensity before focusing.

Antonsen et. al. have suggested that a corrugated channel may be used to generate THz radiation, using either a laser pulse [33] or an electron beam [34] as the driver. This is possible because EM modes in a corrugated channel have a Floquet-type dispersion relation, as shown in Fig. 3.1(b). This means that an EM mode in the channel, defined by a specfic frequency, consists of a sum over spatial harmonics, many of which have subluminal phase velocities. Thus, the group velocity of the ponderomotively driven current will match the phase velocity of a spatial harmonic for a discrete set of modes. This leads to efficient coupling between the driver and modes in this set. Given the correct choice of channel parameters, strong THz production is possible.

Here we perform simulations to model THz production in corrugated plasma channels with realistic density profiles. In Section 3.2 we discuss the excitation and structure of electromagnetic modes in a corrugated channel. In Section 3.3 we give details of the code used to simulate the plasma response of the channel and present test results that verify correct operation of the code. In Section 3.4 we present and discuss results obtained for various system parameters. In Section 3.5 we present our conclusions.

3.2 Excitation of Modes in a Corrugated Channel

3.2.1 Requirements for Excitation

Our goal is to generate THz radiation by passing a laser pulse through a corrugated plasma channel. Since the central frequency of the pump pulse will be

significantly larger than the THz frequencies, we can consider the cycle-averaged current generated by the ponderomotive force of the pulse as the source of the THz. Because of the periodicity of the channel, a component of this current will be associated with one or more electromagnetic modes. The frequency of these modes will be determined by the plasma frequency and other channel parameters.

There are two requirements that must be met in order to successfully generate electromagnetic radiation in a plasma using a laser pulse. Foremost is the requirement that energy must be transferred from the laser pulse to the plasma. The work done by the ponderomotive force on a current is

$$P = \frac{1}{e}\int d^3x \boldsymbol{\nabla} V_p \cdot \boldsymbol{J} = -\int d^3x V_p \frac{\partial n}{\partial t} \,, \tag{3.1}$$

where V_p is the ponderomotive potential, $\boldsymbol{J}$ is the current, e is the charge on an electron and n is the number density of electrons. For power to be transferred from the laser pulse to a mode of the plasma, this mode must have a density perturbation associated with it, i.e. the mode must have non-zero electric field divergence. For electromagnetic modes in a cold, linear fluid plasma, the divergence is of order

$$\boldsymbol{\nabla} \cdot \boldsymbol{E} \sim \mathcal{O}\left(\frac{\omega_p^2}{\omega^2 - \omega_p^2}\frac{|\boldsymbol{E}|}{L}\right) \,, \tag{3.2}$$

where ω is the mode frequency, ω_p is the plasma frequency and L is the characteristic scale length of the non-uniformity of the plasma. For $L \to \infty$, the plasma becomes uniform and we recover the familiar result, $\boldsymbol{\nabla} \cdot \boldsymbol{E} = 0$.

The second requirement is that the group velocity of the laser pulse is phase matched with the phase velocity of the excited modes. This is required for significant excitation to occur, and is achieved in a corrugated channel because the electromagnetic modes of the channel are Floquet-type modes. Each mode of the channel consists of a sum over spatial harmonics, with the wavenumber of each harmonic separated by the wavenumber associated with the density modulations. Thus, a plot of the dispersion relation (See Fig. 3.1(b)) demonstrates the periodicity in k-space characteristic of waves in periodic systems, and the presence of frequency band gaps, in which no mode may propagate. The laser pulse, represented in the figure by a light-line, is phase matched to the mode at several different frequencies, and this allows the excitation of modes at these frequencies.

3.2.2 Parabolic Plasma Channels

In this study we consider cylindrically symmetric corrugated waveguides with densities of the form

$$\frac{n(r,z)}{n_0} = \begin{cases} 1 + \delta \sin\left(k_m z\right) + \dfrac{1}{2}\dfrac{r^2}{r_{ch}^2} & r \le r_c \\ \dfrac{n(r_c,z)}{n_0}\dfrac{r_0 - r}{r_0 - r_c} & r_c < r < r_0 \\ 0 & r \ge r_0 \end{cases} \tag{3.3}$$

Here, n_0 is the on-axis average density, δ is the density modulation amplitude, k_m is the wavenumber of the density modulations, r_{ch} is the channel 'width' that characterizes the density increase with radius, r_c is the radius at which the linear

'cutoff function' in the second line begins and r_0 is the radius at which the density is zero.

In Section 3.3 we will present numerical solutions to Maxwell's equations and the linear fluid equations for TM modes in plasma channels of this form. Before doing so, we use a number of approximations to explore this system analytically. In a cold, non-relativistic and linearly-responding plasma, an electromagnetic mode with small but non-zero electric field divergence and field components (E_r, B_θ, E_z) satisfies the approximate wave equation

$$\left(-\frac{1}{c^2}\frac{\partial^2}{\partial t^2} + \frac{\partial^2}{\partial z^2} + \frac{1}{r}\frac{\partial}{\partial r} r \frac{\partial}{\partial r} - \frac{1}{r^2} \right) E_r = \frac{\omega_{p0}^2}{c^2} \frac{n(r,z)}{n_0} E_r \ , \tag{3.4}$$

where ω_{p0} is the plasma frequency evaluated for the density n_0.

In the case $r_c \to \infty$, only the first part of Eq. (3.3) is relevant and we have a so-called parabolic plasma channel, albeit with axial density modulations. The r and z dependence in this density profile are separable, allowing an analytic solution. In axially uniform channels ($\delta = 0$), we recover the wave equation for modes in a regular parabolic plasma channel. The solution is harmonic in z, and consists of a linear combination of radial eigenmodes, of which there are an infinite number. The solution to Eq. (3.4) for the fundamental radial eigenmode is

$$E_r(r,z,t) = E_0 e^{i(k_z z - \omega t)} \frac{r}{w_{ch}} e^{-r^2/w_{ch}^2}$$

Here, w_{ch} is the mode width given by $8/w_{ch}^4 = (\omega_{p0}^2/r_{ch}^2 c^2)$. The dispersion relation

is

$$\omega^2 = \omega_{p0}^2 + k_z^2 c^2 + \frac{8c^2}{w_{ch}^2}$$

When we include axial modulations ($\delta \neq 0$), applying separation of variables to Eq. (3.4) yields the same ODE in r as for the axially uniform case, and so the ansatz for E_r becomes

$$E_r(r, z, t) = E_0 e^{-i\omega t} f(z) \frac{r}{w_{ch}} e^{-r^2/w_{ch}^2} \ . \tag{3.5}$$

The dispersion relation is now

$$\omega^2 = \omega_{p0}^2 + k_0^2 c^2 + \frac{8c^2}{w_{ch}^2} \ , \tag{3.6}$$

where k_0 is the separation-of-variables parameter. This features in the ODE for $f(z)$:

$$\frac{d^2 f}{dz^2} + k_0^2 f = \frac{\omega_{p0}^2}{c^2} \delta \sin(k_m z) f \ . \tag{3.7}$$

This is the Mathieu equation, and as such cannot be solved analytically. We know from Floquet's theorem however that the solution must be of the form

$$f(z) = e^{ik_z z} \sum_{\alpha=-\infty}^{\infty} A_\alpha e^{-i\alpha k_m z} \ . \tag{3.8}$$

This solution implies a relation $k_z = k_z(k_0)$, and by inversion $\omega = \omega(k_z)$. In general, all coefficients A_α are non-zero, and cannot be found except by infinite recursion.

Substituting Eq. (3.8) into Eq. (3.7), we recover

$$\left[k_0^2 - (k_z - \alpha k_m)^2\right] A_\alpha = \frac{\omega_{p0}^2}{c^2} \frac{\delta}{2i} \left[A_{\alpha-1} - A_{\alpha+1}\right] . \tag{3.9}$$

In the limit $\delta \to 0$, we have $k_0 = k_z - \alpha k_m$ for the harmonic with Fourier coefficient A_α. This is reconciled with the axially uniform solution $k_0 = k_z$ by noting that in this case, $A_\alpha = 0$ for all $\alpha \neq 0$. We construct an approximate dispersion relation for small δ by using the $\delta \to 0$ solution and superimposing on an ω-k_z plot an infinite set of functions of the form

$$\omega = \sqrt{\omega_c^2 + (k_z - \alpha k_m)^2 c^2} \qquad \alpha \in \mathbb{Z} , \tag{3.10}$$

where $\omega_c^2 = \omega_{p0}^2 + 8c^2\gamma/w_{ch}^2$ (γ is the radial eigenmode number). This set of curves deviates from the true dispersion relation near the intersections. At these points, the true dispersion relation will exhibit band gaps in which no propagating wave solution exists. Away from these points, and depending on system parameters, Eq. (3.10) will be a good approximation to the true dispersion relation. A discussion of this, including more accurate calculations of the dispersion relation, is found in Appendix A.

An excited mode in this channel will consist of a sum of spatial harmonics, each harmonic corresponding to a different value of α. The laser pulse traveling at group velocity $v_g \simeq c$ will phase match to one of these harmonics, which will result in the excitation of a mode. As seen in Fig. 3.1(b), this excitation occurs at

frequencies given by the intersection points between the light-line of the laser pulse and the dispersion curves. Replacing k_z with ω/c in Eq. (3.10) gives us the following estimate for the frequencies of the excited modes:

$$\omega = \frac{1}{2\alpha k_m c}(\omega_c^2 + \alpha^2 k_m^2 c^2) \qquad \alpha = 1, 2, \dots \ . \tag{3.11}$$

We refer to modes excited in this way as Floquet modes. Thus, for each radial eigenmode there is a spectrum of Floquet modes generated with frequencies given by Eq. (3.11). We reinforce here that Eq. (3.11) is only strictly valid in the small-δ limit, and the calculated frequencies are only accurate away from the intersections, which indicate the positions of bandgaps in the exact dispersion relation. We note that depending on the choice of modulation period, $\alpha = 1$ does not necessarily label the lowest excited frequency, but this is just a peculiarity of the notation.

3.2.3 Finite Radius Plasma Channels

In this work we do not consider true parabolic plasma channels (i.e. with $n \to \infty$ as $r \to \infty$) beyond the discussion in this section, because the corrugated plasma channels produced in the lab have a density maximum at a finite radius followed by a decrease to zero density (as described by Eq. (3.3). We conclude this section with a brief discussion of two relevant differences between finite-radius channels and parabolic plasma channels.

The first difference is the fact that finite radius channels support a finite number of modes, unlike parabolic plasma channels which support a denumerably infi-

nite number of radial eigenmodes. To estimate the number of modes a channel will support, we consider the local dispersion relation for an axially smooth parabolic channel:

$$\omega^2 = \omega_{p0}^2\left(1 + \frac{r^2}{2r_{ch}^2}\right) + k_z^2c^2 + k_\perp^2c^2 \ . \tag{3.12}$$

If the finite channel supports Γ modes, then we assume that the dispersion relation for these modes is similar to that for the first Γ modes of the parabolic channel, i.e.

$$\omega^2 = \omega_{p0}^2 + k_z^2c^2 + \frac{8\gamma c^2}{w_{ch}^2} \qquad \gamma = 1 \ldots \Gamma \ . \tag{3.13}$$

Combining these two equations and using the relationship between r_{ch} and w_{ch} described in this section, we obtain a simple expression for the perpendicular wavenumber:

$$k_\perp^2 = \frac{4}{w_{ch}^2}\left(2\gamma - \frac{r^2}{w_{ch}^2}\right) \ . \tag{3.14}$$

A mode is bound if the perpendicular wavenumber passes through zero at some radius, and so if the density maximum in the channel exists at radius r_c, modes for which $\sqrt{2\gamma} < r_c/w_{ch}$ will be bound. Alternatively, the number of bound modes is

$$\Gamma = \texttt{int}(r_c^2/2w_{ch}^2) \ . \tag{3.15}$$

The second difference between finite-radius channels and parabolic plasma channels is that in the finite case, the energy in an EM mode may 'leak' through the channel wall and couple to vacuum electromagnetic modes. Thus, an excitation propagating

down the channel will deplete in a finite distance. Of course, this is true for both a laser pulse propagating down a channel (and thus losing energy that may otherwise be converted to plasma waves or THz) and THz modes excited by the pulse. A WKB treatment of laser depletion in a smooth channel may be found in [35]. The rate at which depletion occurs is governed by the transmission coefficient, which in general depends on the height and thickness of the wall of the channel. In the following sections we will study numerically the emission of THz radiation from the sides of a channel described by Eq. (3.3). This emission corresponds to THz modes leaking from the channel in the manner described here.

3.3 Code Details and Verification

3.3.1 Model and Assumptions

The main purpose of this chapter is to describe a series of simulations carried out to determine the characteristics of the THz radiation emission from of a corrugated plasma channel. The THz radiation is the result of currents generated by the ponderomotive force of the laser pulse. For both linearly and radially polarized pulses, the ponderomotive force is cylindrically symmetric, and so we expect the THz modes to be TM modes consisting of components E_r, B_θ and E_z, which satisfy

Maxwell's equations:

$$\begin{aligned}
\frac{1}{c}\frac{\partial E_r}{\partial t} &= -\frac{4\pi J_r}{c} - \frac{\partial B_\theta}{\partial z} \\
\frac{1}{c}\frac{\partial E_z}{\partial t} &= -\frac{4\pi J_z}{c} + \frac{1}{r}\frac{\partial}{\partial r}(rB_\theta) \\
\frac{1}{c}\frac{\partial B_\theta}{\partial t} &= \frac{\partial E_z}{\partial r} - \frac{\partial E_r}{\partial z} \ .
\end{aligned} \tag{3.16}$$

The current components J_r and J_z must be calculated by determining the plasma response to the the ponderomotive force of the laser pulse and the field components determined by the above equations. We do so by modeling the plasma as a linear, non-relativistic, cold electron fluid with a fixed ion background. The evolution of the current $\boldsymbol{J} = -en_0(r,z)\boldsymbol{v}$, where the density $n_0(r,z)$ is given by Eq. (3.3), is determined by solving the momentum equation

$$m_e\frac{\partial \boldsymbol{v}}{\partial t} \simeq -e\boldsymbol{E} - \boldsymbol{\nabla}V_p - \nu m_e\boldsymbol{v} \ , \tag{3.17}$$

where ν is a collisional damping factor and V_p is the ponderomotive potential of the laser pulse. This is typically written as

$$V_p(r,z,t) = \frac{m_e c^2}{2}|\boldsymbol{a}(r,z,t)|^2 \ , \tag{3.18}$$

where $\boldsymbol{a}(r,z,t)$ is the normalized vector potential of the laser pulse. In this work, we consider the laser pulse to be propagating but non-evolving, and so the ponderomotive potential is simply a known function of r and $z - v_g t$ that is substituted into

Eq. (3.17). We use a potential of the form

$$V_p(r, z-ct) = V_{p0} e^{-2r^2/w_{ch}^2} \cos^4\left(\pi \frac{z-ct}{c\tau}\right) \qquad -\frac{c\tau}{2} \leq z - ct \leq \frac{c\tau}{2}\ , \tag{3.19}$$

where τ is the laser pulse duration.

There are conditions that must be satisfied if the system is to be modeled accurately in the manner described above. To begin, the ponderomotive potential must be sufficiently small that both the quiver velocity of the electrons and their cycle averaged motion is non-relativistic. While we do not simulate behavior on the optical timescale, the size of the ponderomotive potential is related to the laser frequency and electric field amplitude, hence the relevance of this condition. The inequality that must hold for both of these conditions to be satisfied is

$$\frac{V_{p0}}{m_e c^2} = \frac{1}{2}|\boldsymbol{a}_0|^2 \ll 1\ , \tag{3.20}$$

where a subscript zero indicates a peak value.

Next, we consider the cold fluid limit. For the plasma to be considered cold, there must be insufficient time for the fluid to thermalize on the timescale of the electron oscillations. This is expressed simply through the inequality

$$k v_{th} \ll \omega\ , \tag{3.21}$$

where $v_{th} \sim \sqrt{k_B T/m_e}$ is the thermal electron velocity and ω and k are a typical frequency and wavenumber of THz radiation. Since the THz is generated by a pulse

moving at $v_g \simeq c$ we expect $\omega/k \sim v_g$, and Eq. (3.21) should be satisfied.

To determine whether we may treat the ions as a fixed, neutralizing background, we must compare the time scale of the laser pulse to the inverse of the ion plasma frequency. Since we are interested in generating radiation in the THz regime, our laser pulse must be short enough that the bandwidth of its envelope encompasses the desired THz frequencies. Moreover, the amplitude of the pulse shape in frequency space must be large at the desired frequencies. In order to generate radiation in the range 1 to 10 THz, our laser bandwidth must be of the order of hundreds of THz, which means we must consider pulse durations of less than 100 fs. By comparison, the inverse ion plasma frequency is 750 fs at $n_0 \sim 1 \times 10^{18}$ cm^{-3} and 7.5 ps at $n_0 \sim 1 \times 10^{16}$ cm^{-3}. Since the inverse ion plasma frequency represents the shortest timescale of ion motion, we conclude that if we restrict ourselves to sufficiently short pulses and sufficiently low densities, we may consider the ions as being stationary.

Finally we consider the validity of the assumption that the laser pulse is non-evolving. This is potentially a stringent approximation, and importantly, we must consider two regimes of validity in dealing with the simulation results. In the first regime, the approximation is valid if the pulse doesn't change shape or amplitude significantly over the length of the simulation window, which will be on the order of tens of density modulations, or a few millimeters. In this case, quantities measured over this distance for a non-evolving laser pulse will match those that would be measured for an evolving laser pulse. We may then estimate the pulse depletion

length by writing down the following energy-conservation expression:

$$\frac{1}{U_L^2}\frac{dU_L}{dt} = \frac{P}{U_L^2} \simeq \frac{\langle P_T \rangle}{U_0^2} \,. \tag{3.22}$$

Here, $U_L(t)$ is the energy in an evolving pulse, $P(t)$ is the power transferred to plasma currents by an evolving pulse, $U_0 = U_L(0)$ is both the initial energy of an evolving pulse and the energy of a non-evolving pulse in our simulation, and $\langle P_T \rangle$ is the average power transferred to the plasma by a non-evolving pulse of energy U_0.

In the linear regime, the pulse energy $U_L(t)$ scales as V_p, and power $P(t)$ lost from the pulse scales as V_p^2. If we assume that the pulse shape doesn't change significantly over the depletion length, then the middle part of Eq. (3.22) is approximately constant. If we are within the first regime of validity, we may estimate the value of this constant using the right-hand-side. The solution to Eq. (3.22) is

$$\frac{U_L(t)}{U_0} = \left(1 + \frac{\langle P_T \rangle t}{U_0}\right)^{-1} \,. \tag{3.23}$$

Here we identify the depletion length of the pulse $L_D = cU_0/\langle P_T \rangle$.

The second regime of validity concerns whether or not the above depletion estimate is accurate, because of pulse evolution effects that occur on scale lengths longer than the simulation length, but shorter than the estimated depletion length. These can be both linear shape evolution effects, such as group velocity dispersion, and non-linear evolution effects such as pulse compression due to density-perturbation-induced group velocity variation, and redshifting due to phase velocity variation

[36]. We note that within our model, L_D scales inversely with pulse energy, and results for different pulse energies can be found by rescaling the result of a single run with a reference pulse energy. Therefore, we must consider the validity of the approximation for both the depletion length obtained from our simulation results, and for depletion lengths obtained through rescaling our results. Conflicts in this area will be discussed when we present rescaled depletion estimates in Section 3.4.

Returning to the first regime of validity, there are several pulse evolution effects to consider. First we consider pulse depletion due to plasma wake excitation. In an axially uniform plasma, this is maximized when the pulse length matches the wavelength of the plasma oscillations. For plasma densities of 5×10^{17} to 2.5×10^{18} cm^{-3}, this occurs for pulse lengths 160 to 70 fs respectively. The depletion length for a pulse initially at linear resonance in the weakly relativistic regime ($a_0^2 \ll 1$) is given by[36, 37]

$$k_p L_{dp} \simeq \frac{17.4}{a_0^2}\left(\frac{k_0}{k_p}\right)^2, \tag{3.24}$$

where k_0 is the central wavenumber of the laser pulse and $k_p = \omega_{p0}/c$. For a laser energy of 0.01 J, wavelength of 800 nm and pulse width of 15 μm ($a_0 \simeq 0.1$), the depletion lengths for the given density range go from about 3300 to 300 cm. For a laser energy of 0.5 J ($a_0 \simeq 0.8$), which is the energy to which we intend to rescale our results, the depletion lengths range from around 70 to 6 cm. We note that this is the depletion length for a pulse with initial length equal to the plasma wavelength. Our pulse is somewhat shorter than the ambient plasma wavelength, and since the plasma wavelength in our simulation changes because of the density modulations,

the pulse spends some time even further away from resonance. Hence, we expect the pulse depletion length in a modulated channel to be larger than that predicted by Eq. (3.24).

Another effect to consider is group velocity dispersion (GVD). This effect may be estimated by considering the range of group velocities in a pulse of length $c\tau$ in configuration space and its corresponding length in Fourier space [38]. The propagation distance over which the pulse doubles in length is given by

$$L_{GVD} \simeq k_0 c^2 \tau^2 \left(\frac{k_0}{k_p}\right)^2 . \tag{3.25}$$

For our given density range, L_{GVD} ranges from about 600 to 100 cm, which is significantly longer than the simulation length.

Although GVD happens relatively slowly, the pulse may still disperse due to the Floquet structure of the EM modes in our system. The laser pulse is composed of Floquet modes, meaning that each mode consists of a set of spatial harmonics. For any given mode the group velocity of each spatial harmonic is the same, however if the bandwidth of the pulse overlaps a band gap, some of the modes will have significantly different group velocities than they would in a pulse traveling in a uniform channel, leading to rapid pulse deformation.

This, however, is not an issue in our system. The pulse bandwidth extends over several bandgaps, which at high frequency are separated by $\omega \simeq k_m c/2$. The bandgaps themselves however, have essentially zero-width in the high frequency regime. This may be seen by referring to the calculation performed in the Appendix,

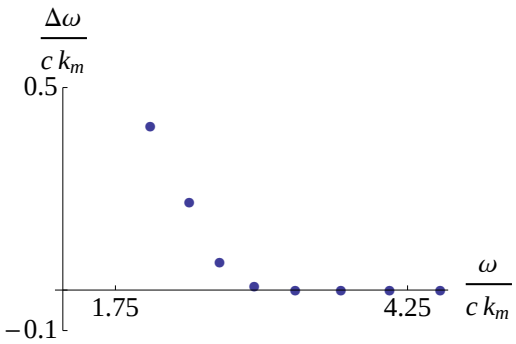

Figure 3.2: Plot of normalized bandgap size as a function of normalized central bandgap frequency, obtained from the numerical calculation of the dispersion relation, performed in the Appendix. Note that the bandgap size vanishes rapidly with increasing frequency, at a point far below the typical frequencies associated with an optical pulse.

the relevant results of which are displayed in Fig. 3.2. Note that the frequency at which the bandgap size vanishes is significantly lower than the laser frequency, hence the approximate dispersion relation in Eq. (3.10) becomes exact in the high-frequency limit. Our conclusion therefore is that although an optical-frequency pulse in a corrugated system will be composed modes consisting of several spatial harmonics, the dispersion structure of each of the harmonics in a mode will be the same (up to a k offset) as those of the corresponding mode from a pulse in an axially uniform channel.

In order to reinforce the validity of the non-evolving pulse approximation, we perform simulations with the code WAKE [39] using our channel parameters over many Rayleigh lengths. Plots (a) to (c) of Fig. 3.3 show the Fourier transforms of the pulse envelope from such a simulation, conducted for a modulated plasma channel with central density $n_0 = 10^{18}$ cm^{-3}, modulation amplitude $\delta = 0.9$ and modulation wavelength 50 μm for a pulse of length 50 fs, width 15 μm, wavelength 800 nm

and normalized vector potential amplitudes of $a_0 = 0.2$, $a_0 = 0.4$ and $a_0 = 0.8$. As can be seen from the plots, the frequency content of the weakest pulse changes little over a length of 40 Rayleigh lengths, which corresponds to about 15 cm for a 15 μm-width pulse. Such a pulse is consistent with the first regime of validity. Over this length, the frequency content of a stronger pulse changes significantly. In Fig. 3.3(b), there appears to be some pulse broadening, whereas in Fig. 3.3(c), significant pulse depletion has occurred. In Fig. 3.3(d), we see that the frequency content of even a strong pulse changes little over one Rayleigh length, and so it is marginally consistent with the first regime of validity.

From the preceding discussion, we conclude that we can obtain useful results from our model. In particular, the first regime of validity of the non-evolving approximation holds over a wide range of parameters. Care must be taken when using the results to obtain estimates of the depletion length, since violations of the second regime of validity may occur. In the case of low energy pulses, the depletion length L_D often exceeds the group velocity dispersion length L_{GVD}, while in the case of high energy pulses, significant changes in pulse shape occur despite the the depletion length being much shorter. In this discussion we have neglected instabilities (such as the Raman instability) that cause the pulse shape to change. These can be ignored for a 50 fs laser pulse, and we consider any effect they may have as a subject for future study.

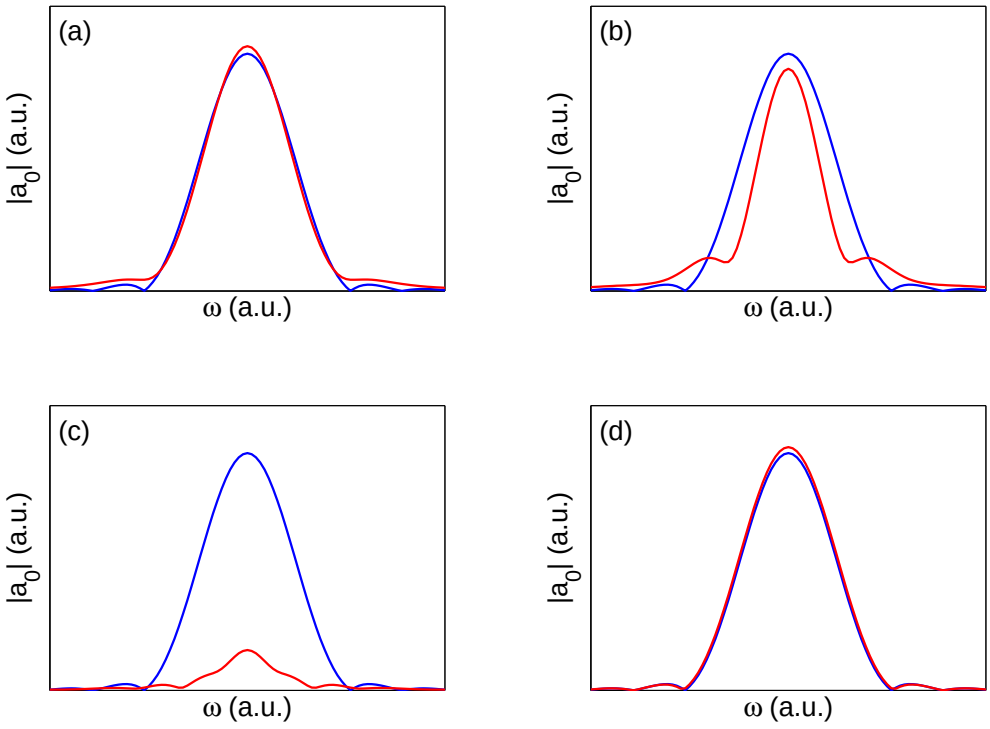

Figure 3.3: Plots of the Fourier transforms of 50 fs laser pulses with wavelength 800 nm and spot size 15 μm, recorded initially (blue) and after propagation for 40 Rayleigh lengths for normalized vector potential amplitudes of (a) $a_0 = 0.2$, (b) $a_0 = 0.4$ and (c) $a_0 = 0.8$. These potentials correspond to pulse energies of 0.03, 0.1 and 0.5 J respectively. Plot (d) is for $a_0 = 0.8$ for a pulse propagating over one Rayleigh length. These plots were generated using the simulation WAKE.

3.3.2 Algorithm

The fact that the plasma responds in a linear fashion allows us to use a simple algorithm to simulate the time evolution of the fields and currents. The electric and magnetic field components are solved on a two-dimensional Yee grid [40] as follows:

$$\begin{aligned}
\frac{[E_r]^{n+\frac{1}{2}}_{i,j+\frac{1}{2}} - [E_r]^{n-\frac{1}{2}}_{i,j+\frac{1}{2}}}{c\Delta t} &= -\frac{4\pi[J_r]^n_{i,j+\frac{1}{2}}}{c} - \frac{[B_\theta]^n_{i,j+1} - [B_\theta]^n_{i,j}}{\Delta z} \\
\frac{[E_z]^{n+\frac{1}{2}}_{i+\frac{1}{2},j} - [E_z]^{n-\frac{1}{2}}_{i+\frac{1}{2},j}}{c\Delta t} &= -\frac{4\pi[J_z]^n_{i+\frac{1}{2},j}}{c} + \frac{(i+1)[B_\theta]^n_{i+1,j} - i[B_\theta]^n_{i,j}}{(i+\frac{1}{2})\Delta r} \\
\frac{[B_\theta]^{n+1}_{i,j} - [B_\theta]^n_{i,j}}{c\Delta t} &= \frac{[E_z]^{n+\frac{1}{2}}_{i+\frac{1}{2},j} - [E_z]^{n+\frac{1}{2}}_{i-\frac{1}{2},j}}{\Delta r} - \frac{[E_r]^{n+\frac{1}{2}}_{i,j+\frac{1}{2}} - [E_r]^{n+\frac{1}{2}}_{i,j-\frac{1}{2}}}{\Delta z} \,.
\end{aligned} \tag{3.26}$$

Here, n in the time index, i is the radial index and j is the axial index. The magnetic field resides at gridpoints labeled by integers, while the r and z components of the remaining quantities are offset by one-half step in z and r respectively. The electric field components are evaluated at half-integer timesteps while the magnetic field and the current is evaluated at integer timesteps. The current can be treated in this way because of the absence of the convective term in the momentum equation, and because the ponderomotive force is a known function $V_p(r, z - v_g t)$ and so can be evaluated at any point in space and time.

The damping term in Eq. (3.17) requires a manipulation to allow the evaluation of the current. Writing $\boldsymbol{v}^{n+\frac{1}{2}} = \frac{1}{2}(\boldsymbol{v}^n + \boldsymbol{v}^{n+1})$ and approximating the derivative as a central difference centered around $n + \frac{1}{2}$, we have

$$\left(1 + \frac{\nu\Delta t}{2}\right) m_e \boldsymbol{v}^{n+1} = \left(1 - \frac{\nu\Delta t}{2}\right) m_e \boldsymbol{v}^n - \Delta t\left(e\boldsymbol{E}^{n+\frac{1}{2}} + \boldsymbol{\nabla} V_p^{n+\frac{1}{2}}\right) . \tag{3.27}$$

From this, it is a simple matter to calculate the current components $[J_r]^n_{i,j+\frac{1}{2}}$ and $[J_z]^n_{i+\frac{1}{2},j}$ via $\boldsymbol{J} = -en_0(r,z)\boldsymbol{v}$.

The Yee algorithm is known for having lenient stability requirements compared to algorithms of similar complexity defined using a common grid for all field components. A necessary condition for stability is the Courant-Friedrichs-Lewy (CFL) condition. Informally, this states that a timestep must be smaller than the time taken for a disturbance to propagate from one gridpoint to the next. For Maxwell's equations in vacuum on a two dimensional Cartesian mesh with step sizes Δx and Δz, this condition is

$$\frac{1}{c}\frac{1}{\Delta t} \geq \sqrt{\frac{1}{\Delta x^2} + \frac{1}{\Delta z^2}}\,. \tag{3.28}$$

The CFL condition is necessary but not sufficient for stability, and to study the stability our algorithm we resort to a Von-Neumann analysis of Maxwell-fluid equations, again in a two-dimensional Cartesian system, and without considering the damping term or ponderomotive force of Eq. (3.27). This analysis involves performing a spatial Fourier transform on Eq. (3.26) and Eq. (3.27), and finding a solution of the form $\boldsymbol{U}^{n+1} = \underline{\boldsymbol{G}} \cdot \boldsymbol{U}^n$, where $\boldsymbol{U}^n = (E_x^{n-\frac{1}{2}}, B_\theta^n, E_z^{n-\frac{1}{2}}, v_x^n, v_z^n)^{\mathrm{T}}$. $\underline{\boldsymbol{G}}$ is the amplification matrix for the algorithm, and the condition for stability is that the magnitude of the eigenvalues of this matrix are less than or equal to unity.

This problem is not tractable analytically. We resort to finding the eigenvalues numerically and displaying them as stability curves. For timesteps marginally satisfying the CFL condition most eigenvalues have magnitude unity, indicating neutral stability. The exception is for the eigenvalue associated with $E_x^{n-\frac{1}{2}}$, where an un-

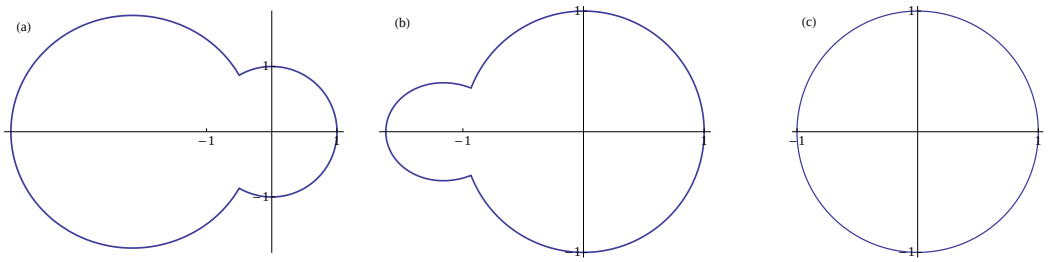

Figure 3.4: Stability surface cross sections evaluated at $k_z \Delta z = \pi$ for the eigenvalue associated with $E_x^{n-\frac{1}{2}}$ of the amplification matrix for a Cartesian two-dimensional Maxwell-Fluid system without damping. We have (a) $dt = dt_{CFL}$, (b) $dt = 0.95\, dt_{CFL}$ and (c) $dt = 0.9\, dt_{CFL}$.

stable region is present. This is most easily viewed by looking at a cross section of the stability surface for this eigenvalue, evaluated at $k_z \Delta z = \pi$. The results for this are found in Fig. 3.4. We note that only a small safety factor of ~ 0.9 is required to bring the algorithm to a state of neutral stability.

The stability analysis performed here ignores various aspects of our simulation that will affect stability, including boundary conditions, curvilinear effects and the inclusion of a damping term. Nonetheless, our code performs in a stable manner with a safety factor of 0.95 over a sufficiently long period as to obtain meaningful results.

3.3.3 Implementation

We implement this algorithm using the relatively new NVidia Tesla General Purpose Graphical Processing Units [41] designed for use in desktop-scale parallel computation. We choose a spatial step size by identifying the various length scales in the system (the plasma wavelength, the modulation wavelength, etc) and choosing

a grid size that resolves the smallest of these. Then, we use the CFL condition with our safety factor of 0.95 to calculate the required timestep.

The radial boundary conditions for a cylindrical coordinate system at the origin are $E_r = B_\theta = J_r = 0$ and $\partial E_z/\partial r = \partial J_z/\partial r = 0$. Noting that the structure of a Yee cell means that we only need to specify E_z and J_z at the radial boundaries, we choose the inner simulation boundary to be at $r = -\Delta r/2$ and set $[E_z]^{n+\frac{1}{2}}_{-\frac{1}{2},j} = [E_z]^{n+\frac{1}{2}}_{+\frac{1}{2},j}$ and $[J_z]^{n}_{-\frac{1}{2},j} = [J_z]^{n}_{+\frac{1}{2},j}$.

For the outer radial boundary, we use a Perfectly Matched Layer (PML) [42]. The purpose of this is to ensure that any THz radiation that escapes radially from the channel will not be reflected from the boundary. For simplicity, we implement a Cartesian PML and choose the radial system size to be large enough that curvilinear effects are minimized in the region where the PML is present. This means that we replace the radial derivatives in our equations with

$$\frac{\partial}{\partial r} \rightarrow \frac{1}{1 + i\sigma(r)/\omega}\frac{\partial}{\partial r}\,, \tag{3.29}$$

where $\sigma(r)$ is the PML strength factor that vanishes for some $r < r_{PML}$. This leads to plane wave modes that develop complex wavenumbers in the region $r > r_{PML}$:

$$\exp\left[i(kr - \omega t)\right] \rightarrow \exp\left[i(kr - \omega t)\right]\exp\left[-\sigma(r)r/c\right]\,. \tag{3.30}$$

We choose a parabolic strength factor $\sigma(r) \propto (r - r_{PML})^2$. This is to avoid numerical reflections generated by a sudden change from vacuum to PML. The width of the

PML is chosen to be two plasma wavelengths, since the plasma frequency is similar to the frequencies of the THz modes we expect to generate. This, along with setting the maximum value of $\sigma(r)$ to several times the plasma frequency, will allow sufficient space for the outward propagating modes to decrease to negligible amplitude.

For the axial boundary, we use periodic boundary conditions. This allows the laser pulse to pass through the system several times, giving time for transients to die away before any THz measurements are made. This process is aided by ramping the ponderomotive potential amplitude V_{p0} from zero to full strength over the course of one pass of the pulse. The collisional damping term in Eq. (3.17) is set so as to reduce the laser wake significantly after one laser pass, thus preventing overlap of the pulse with its wake from the previous pass. For these simulations, we use $\nu = 8c/L_S$, where L_S is the chosen system length. For a density of $n = 10^{18}$ cm^{-3} and a system length of .32 cm (both typical values), this is 1.3 percent of the plasma frequency.

3.3.4 Post-Processing

Once the laser pulse has passed through the system several times, we must determine the amount of THz radiation emitted. On the last pass of the laser pulse, we store various field quantities for this purpose. We store for all z and t the r-integral of the product of the radial part of the ponderomotive potential and the current divergence for the purpose of calculating the power transferred to the plasma by the laser pulse. We also store for all z and t the z-component of the

electric field and the magnetic field at a fixed radius R outside the channel for the purpose of calculating the radial Poynting flux, and for all r and t the r-component of the electric field and the magnetic field at a fixed axial position Z for the purpose of calculating the radial Poynting flux.

Storing information about individual timesteps allows us to calculate time-averaged quantities as sums in frequency space. Writing the ponderomotive potential as $V_p(r, z - ct) = V_{p0} g(z, t) h(r)$, we have

$$\begin{aligned}
\langle P_T \rangle &= \int \frac{d\omega}{2\pi}\, p_T = \int \frac{d\omega}{2\pi} \Big(- \frac{2\pi V_{p0}}{eT} \int dz\, \widetilde{g}(z, \omega) \int r dr\, h(r) \boldsymbol{\nabla} \cdot \widetilde{\boldsymbol{J}}(r, z, -\omega) \Big) \\
\langle P_r \rangle &= \int \frac{d\omega}{2\pi}\, p_r = \int \frac{d\omega}{2\pi} \Big(- \frac{c}{2T} \int R dz\, \widetilde{E}_z(R, z, \omega) \widetilde{B}_\theta(R, z, -\omega) \Big) \\
\langle P_z \rangle &= \int \frac{d\omega}{2\pi}\, p_z = \int \frac{d\omega}{2\pi} \Big(\frac{c}{2T} \int r dr\, \widetilde{E}_r(r, Z, \omega) \widetilde{B}_\theta(r, Z, -\omega) \Big) \,, \qquad (3.31)
\end{aligned}$$

where tilde indicates a Fourier transform in time and the lower case letters/quantities in parentheses are power densities in frequency space. For the simulation, integrals are replaced by the appropriate sums and T is the duration of one laser pulse pass. Studying the power densities will reveal the frequencies of the excited modes. In addition to calculating these quantities, we may gain information about the spatial structure of the modes by looking at the k-z Fourier transform of the stored field quantities.

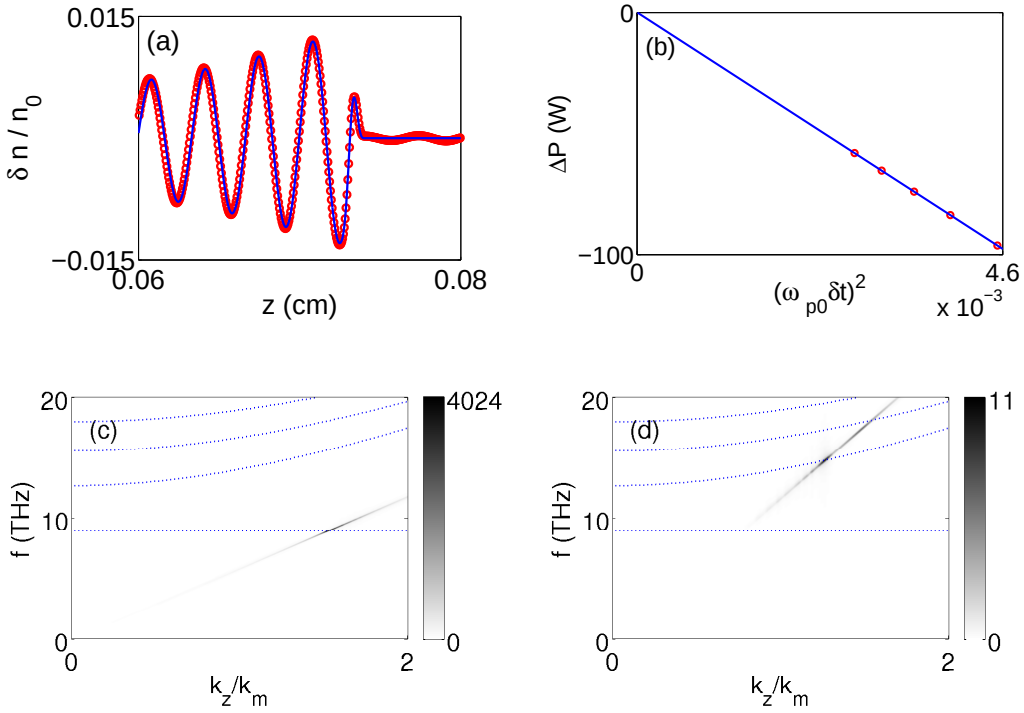

Figure 3.5: Plots from a simulation of a laser pulse passing through a uniform plasma showing (a) density perturbation $\delta n/n_0$ calculated analytically (blue line) and numerically (red circles) for a uniform plasma and (b) difference between power input and output as a function of normalized stepsize squared. Plots of $\widetilde{E}_z(k_z, \omega)$ from a simulation of a laser pulse passing through a parabolic plasma channel evaluated for (c) $v_g = c$ at $r = 0$ and (d) for $v_g = 2c$ at $r > r_0$.

3.3.5 Code Verification

Before using the code to generate results, we must ensure correct operation. We do this by comparing numerical results to analytic results, and by verifying energy conservation in the small-stepsize limit. Various plots associated with the first stage of code verification are shown in Fig. 3.5.

Fig. 3.5(a) shows the linear density perturbation as a function of axial distance calculated analytically (blue line) and numerically (red circles). In the simulation,

the laser pulse is allowed to pass through the system several times before the density perturbation is recorded, and the small oscillations leading the pulse are the damped wake from the previous laser pass. Fig. 3.5(b) shows the quantity $\Delta P = \langle P_T \rangle - \langle P_L \rangle$ as a function of the square of the normalized timestep, where $\langle P_L \rangle$ is the power extracted from the system due to the collisional damping term. The power difference ΔP varies linearly, as expected from the second-order numerical error associated with the chosen algorithm. It converges in the limit $dt \to 0$ to a value six orders of magnitude less than the individual power measurements, hence we conclude that in this case, our code displays the appropriate energy conservation properties.

In Figures 3.5(c) and 3.5(d) we see Fourier transforms of E_z generated by a laser pulse in an axially uniform parabolic plasma channel. In both plots the horizontal line indicates the plasma frequency on axis, while the curved lines are the dispersion curves for the first three radial eigenmodes. In 3.5(c), the transform is taken on axis. There is a strong excitation at the plasma frequency, as evidenced by the peaks of $\widetilde{E}_z(k_z, \omega)$ at the intersection of the light line and the plasma frequency, which is consistent with the expectation that strong excitation requires phase matching.

In 3.5(d), the transform is taken at a radius outside the plasma channel and with the laser pulse group velocity set to $v_g = 2c$. While not physically realistic, this is possible in the code because the pulse is modeled as a force that depends on $z - v_g t$, where v_g is a free parameter. Here there are several excitations, corresponding to the lowest frequency EM modes in the channel. There is no plasma wave excitation, since the density at the point of measurement is zero. While we match the laser

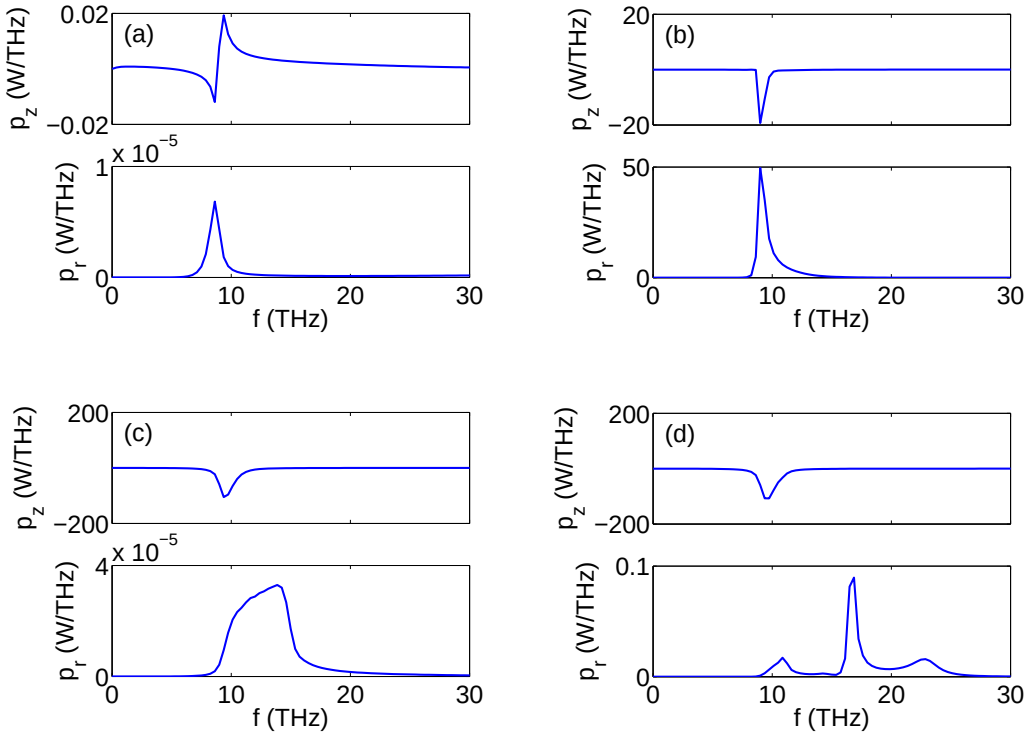

Figure 3.6: Axial and radial power flow density in frequency space for (a) uniform plasma, (b) $\delta = 0.05$ axial corrugations but no radial density dependence, (c) a finite radius plasma channel with no axial corrugations and (d) a finite radius plasma channel with $\delta = 0.05$ axial corrugations.

pulse spot size to the fundamental mode width (which is a requirement if our non-evolving laser pulse assumption is to be valid), the ponderomotive force consists of a broad spectrum of radial eigenmodes. Since this is responsible for driving the current, we expect to see excitations above the fundamental.

Now we look at axial and radial average power outputs recorded for the cases of $\delta = 0$ and $\delta = 0.05$ in both radially uniform plasmas and finite radius plasma channels. We choose a density of $n_0 = 10^{18}$ cm^{-3}, 16 corrugations of length 50 μm and a laser pulse mode width of $w_{ch} = 15$ μm. In the radially uniform case, the mode width doesn't carry its usual physical interpretation, and is to be thought of

as just a length scale. In all cases, we use a laser pulse with an energy of $U_L = 0.01$ J and we choose cutoff parameters $r_c = 2w_{ch}$ and $r_0 = 3w_{ch}$.

In 3.6(a), we see a very small excitation at around the plasma frequency (which for our chosen density is 9.0 THz). This is to be expected, since in a uniform plasma we expect no EM excitation, and plasma waves have no Poynting flux. In 3.6(b), we see much larger excitations. The radial Poynting flux is an EM mode, since the plasma density is zero at the point of measurement. The nature of the axial excitations is not clear, since in a channel with non-uniform density, the magnetic fields generated by the plasma wave currents don't sum to zero. In these simulations however, the axial Poynting flux is of less importance than the radial Poynting flux. This is because the periodic boundary conditions make our channel infinite in length, and so even if we could isolate the contribution to the axial flux from EM modes, the recorded value would not be an accurate representation of the amount of THz exiting the end of a finite-length waveguide.

In 3.6(c), we again see an excitation in the axial power flow plot. There is no significant excitation in the radial plot, consistent with $\delta = 0$. In 3.6(d), we see excitations between 10 and 20 THz in the radial power flow plot. For comparison, the first seven predicted Floquet frequencies for the fundamental radial eigenmode are 12.7, 13.5, 15.4, 16.4, 17.7, 20.2 and 22.9 THz. We note that a much smaller amount of radiation escapes radially than in the case of 3.6(b). This is because the generated modes are unbound, and have a Rayleigh length much shorter than the simulation length.

Finally, we study the power balance in the four scenarios in Fig. 3.6. The

Figure	$\lim_{\Delta t \to 0} \Delta P$ (W)	$\lim_{\Delta t \to 0} \langle P_r \rangle$ (W)
3.6(a)	0.117	0.000164
3.6(b)	306	305
3.6(c)	0.0930	0.000276
3.6(d)	1.47	0.404
$\delta = 0.9$	475	472

Table 3.1: Values of the difference between power input and output ΔP, and the radial power flow $\langle P_r \rangle$, for the different scenarios in Fig. 3.6. For comparison, the result for a full-strength ($\delta = 0.9$) channel is listed.

results are listed in Table 3.1. In the case of Figures 3.6(a), 3.6(c) and 3.6(d), we see that the different measures produce somewhat different results. This is of no concern however, since the ΔP results are six orders of magnitude less than their respective values of $\langle P_T \rangle$ and $\langle P_L \rangle$, and are probably influenced by floating point error. Accordingly, the result for 3.6(b) is much more accurate. A similar level of accuracy is demonstrated in the last row of the table, in which we record the results for a 'full-strength' corrugated channel of the type that will be studied in the next section.

3.4 Simulation Results

We begin by presenting results for the total power output calculated from the simulation for various densities and laser spot sizes. Fig. 3.7 contains the average radial power exiting the side of the waveguide as well as the average axial power flow, the percentage of laser energy converted to THz and the average angle of emission. These results are recorded for a range of densities and mode widths, for a laser pulse energy $U_0 = 0.01$ J, modulation amplitude $\delta = 0.9$ and density cutoff parameters

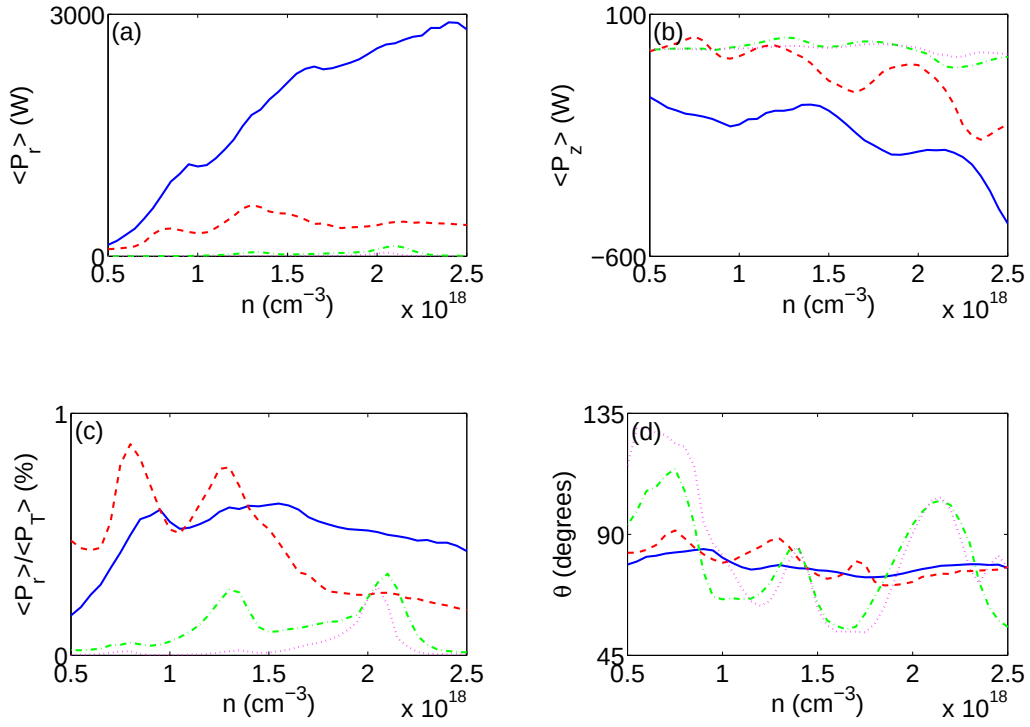

Figure 3.7: Plots involving various quantities as a function of density for channel widths $w_{ch} = 15$ μm (blue, solid), $w_{ch} = 25$ μm (red, dashed), $w_{ch} = 50$ μm (green, dash-dot) and $w_{ch} = 75$ μm (magenta, dotted). The quantities are (a) average power flow in the radial direction, (b) average power flow in the axial direction, (c) percentage of laser energy converted to THz and (d) angle between the Poynting vector measured outside the channel and the axis.

$r_c = 2w_{ch}$ and $r_0 = 3w_{ch}$. The pulse length is 50 fs and the optical wavelength (which is used in conjunction with U_0 to determine the peak ponderomotive potential) is 800 nm. The density modulation period is 50 μm and the total system length is .32 cm.

In Fig. 3.7(a) we see the radial power flow as a function of average on-axis density, measured for several different mode widths. We see that the largest THz generation occurs for small mode widths. In general, this occurs because we have kept the energy content of the pulse fixed, and so the peak ponderomotive potential

is larger in the case of smaller mode width. The amount of THz produced increases with density, because the work done on the plasma by the laser pulse is larger for larger density.

In Fig. 3.7(b) we see the axial power flow as a function of average on-axis density, measured for several different mode widths. This quantity may take a negative value since the mode may propagate either way along the channel. Backwards propagating waves come from lightline intersections with the dispersion function when its gradient is negative. We see that the axial flow is typically several times smaller than the radial flow, which is a desirable property because of the difficulties in calculating accurately the THz output from the end of a real channel.

In Fig. 3.7(c) we plot the ratio of $\langle P_r \rangle$ to $\langle P_T \rangle$ as a percentage, which serves as an estimate of the fraction f of laser energy that is converted to THz. This can be seen by writing $f \sim \langle P_r \rangle \tau_D / U_0$ and replacing the expression for the depletion time τ_D with that calculated in Section 3.3. Importantly, both $\langle P_r \rangle$ and $\langle P_T \rangle$ scale like V_p^2 in the linear regime, which means that the fraction of laser energy converted to THz is independent of the pulse energy.

We may now estimate the amount of THz generated. The peak value of f in Fig. 3.7(c) is less than one percent. We note however that these results are from a system with artificially high collisional damping, which in these simulations is $\nu = 8c/L_S$, and so we expect the recorded conversion fraction is lower than that for a real channel. Extrapolation from a study of the variation of f with damping rate, along with crude estimates of the effect of damping (for example multiplying f by $\exp(\nu r_0)$) suggest that at most, the presence of damping reduces f by a factor

	$U_0 = 0.01$ J		$U_0 = 0.5$ J	
w_{ch} (μm)	E_{THz} (mJ)	L_D (cm)	E_{THz} (mJ)	L_D (cm)
15	0.12	1000	6.1	22
25	0.15	3700	7.8	76
50	0.054	16000	2.7	340
75	0.0034	37000	0.17	780

Table 3.2: Values of energy emitted in THz radiation and laser pulse depletion length for two different values of pulse energy and various mode widths. These quantities are calculated for a density of 1.3×10^{18} cm^{-3}, corresponding to peaks in Fig. 3.7(c).

of two. Using a conversion fraction of $2f$, the values of the pulse depletion length are displayed in Table 3.2 for different mode widths. The depletion length was calculated for a $U_0 = 0.01$ J pulse and rescaled for a $U_0 = 0.5$ J pulse at a density of 1.3×10^{18} cm^{-3}, which corresponds to a peak in Fig. 3.7(c) for both small and large mode widths. The rescaling was accomplished using the fact that L_D scales like V_p^{-1}.

The results in Table 3.2 must be discussed in the context of the non-evolving pulse approximation, details of which are found in Section 3.3. The depletion lengths calculated for the low energy pulse are longer than the group velocity dispersion lengths, although the amount of THz produced in so low that this case is of little interest. The high energy pulse produced sufficient THz to be of interest, although for small mode widths the plasma response is weakly relativistic ($a_0 = 0.8$ for the 15 μm case), and so the pulse evolution will not be represented accurately by Eq. (3.23).

During non-linear pulse evolution in an axially uniform channel however, the pulse initially compresses due to the reduction in plasma density behind the pulse. During this phase, the depletion rate increases. At later times the pulse lengthens

and the depletion rate is reduced. Let us assume that the qualitative features of non-linear pulse evolution in a corrugated channel are similar to those in an axially uniform channel. Then, since most of the pulse energy is depleted during the first phase of pulse evolution and the THz production rate is larger for stronger pulses, the values of L_D for the 0.5 J pulse serve as an upper bound for an effective depletion length, defined to be the length over which significant THz production occurs in a real channel. We note that linear features of pulse evolution in a corrugated channel, such as the fact that the depletion length is longer than that given in Eq. (3.24) due to variation of plasma wavelength with density modulations, are already accounted for in the depletion estimates given in Table 3.2.

An interesting feature of Fig. 3.7(c) is the presence of peaks in the value of f at different densities. There are two possible reasons for this density-dependent enhancement of THz output. The first reason is that the angle of the Poynting vector outside the channel is not always perpendicular, as seen in Fig. 3.7(d). The reason for this will be discussed later in this section. The result is that $\langle P_r \rangle$ is enhanced when the measured angle is close to 90 degrees. Multiplying the data in Fig. 3.7(c) by the sine of the angles in Fig. 3.7(d) reveals however, that this effect in minimal.

The second reason is related to enhanced coupling of the laser to THz modes at the so-called π and 2π points. These are the points on the dispersion curves at which $k/k_m = n$ and $k/k_m = 2n$ respectively. Antonsen et. al. [33] discuss the importance of these special points in their treatment of the delta-function periodic profile. Of central importance in their calculation is a coupling constant that is

proportional to the z-average of the electric field divergence, i.e.

$$I = \frac{1}{d}\int_0^d dz\, \boldsymbol{\nabla}\cdot\boldsymbol{E}\ , \tag{3.32}$$

where $d = 2\pi/k_m$.

We may evaluate this for our density profile by assuming that the electric field divergence takes the form of a Floquet solution, as is found in Eq. (3.8). Adding this to its complex conjugate and integrating over one period of the structure yields

$$I = \sum_{\gamma=-\infty}^{\infty}\left(2\,\mathrm{Im}\{B_\gamma\}\frac{\cos(kd)-1}{(k-\gamma k_m)d} + 2\,\mathrm{Re}\{B_\gamma\}\frac{\sin(kd)}{(k-\gamma k_m)d}\right). \tag{3.33}$$

The π (2π) points occur when $kd = n\pi$ for odd (even) n. The second term in this sum is a maximum when $n = 2\gamma$, which only occurs at a particular 2π point, and is zero for all other 2π points and all π points. Conversely, the first term is an extremum for all π points and vanishes for all 2π points. Because the dispersion curves, and hence the lightline intersections, shift with changing density, there are special densities at which the lightline intersects a dispersion curve at a π or 2π point. We can estimate the densities at which the coupling is maximum by combining the trigonometric functions in Eq. (3.33) with Eq. (3.11), which predicts the frequencies of generated THz modes. The results depend on the lightline intersection number, which must be determined by a frequency-space analysis of the system, and on the Fourier coefficients B_γ, which are not known. This makes it impossible to determine exactly the coupling as a function of density, however for the first lightline intersection in

a 50μm channel (this choice is justified later), the 2π points occur at densities of 1.3×10^{18} and 2.2×10^{18} cm^{-3}, while the π points occur at densities of 8.5×10^{17} and 1.7×10^{18} cm^{-3}. Comparing these number to Fig. 3.7(c), we see that the enhanced THz output occurs at densities corresponding to 2π point intersections.

The results presented thus far have been for a fixed pulse length of 50 fs. For the purpose of optimizing THz production, it is useful to study the effects of pulse length on power output. Fig. 3.8 contains the results of a study conducted for pulse lengths ranging from 6 to 150 fs, again for a pulse energy of $U_0 = 0.01$ J, modulation amplitude $\delta = 0.9$, density cutoff parameters $r_c = 2w_{ch}$ and $r_0 = 3w_{ch}$, optical wavelength 800 nm, density modulation period is 50 μm and total system length is .16 cm. The smaller system length is necessary because a larger resolution is required to resolve the shorter pulse lengths considered. Since we choose the damping to vary with inverse simulation length, the result of this change is to reduce the amount of THz radiation that escapes from the channel. Note that this reduction would not appear in an experimental result, in which the damping rate would be independent of simulation length.

The prominent feature of Fig. 3.8(a) is the decrease in power output with increasing pulse length over much of the domain, with a maximum at $\tau \simeq 12$ ps. The decrease occurs since the ponderomotive force is stronger for smaller pulse lengths, both because the gradient of V_p scales like $1/\tau$ and because the pulse energy is fixed, leading to a variable peak ponderomotive potential. In Fig. 3.8(b) we see the average power transferred from the laser pulse to the plasma. This is linear in the range 25 to 100 fs, with some deviation outside this range. This quantity varies

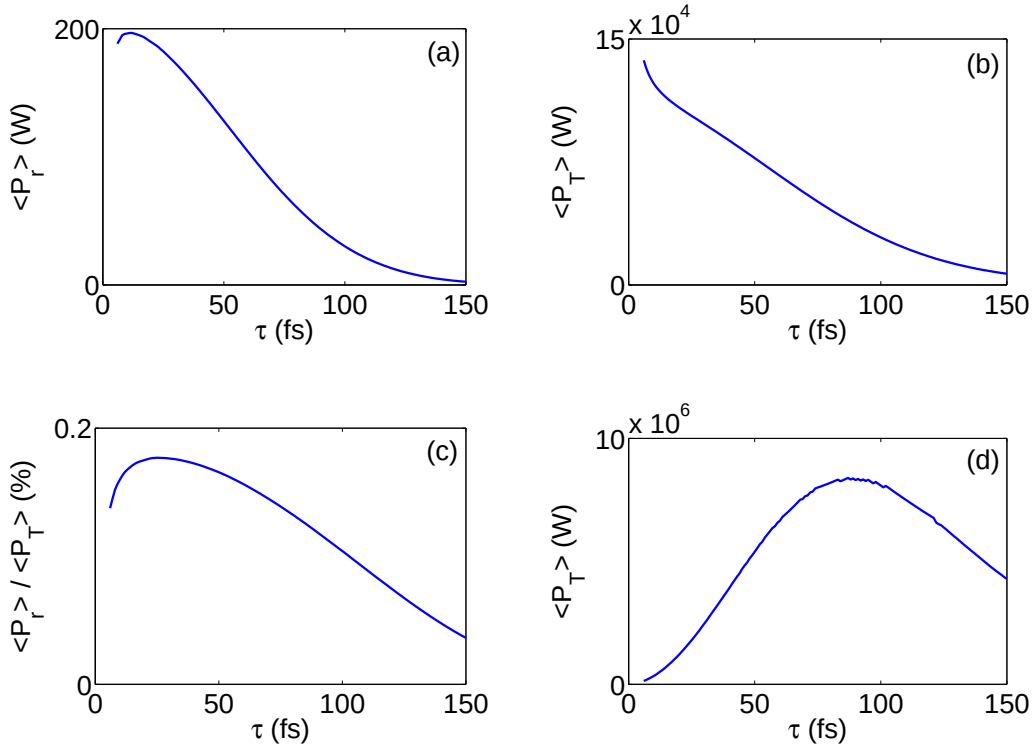

Figure 3.8: Plots involving various quantities as a function of pulse duration for density $n_0 = 1.25 \times 10^{18}$ cm^{-3} and channel width $w_{ch} = 25$ μm. The quantities are (a) average power flow in the radial direction, (b) average power transferred from the laser pulse to the plasma, (c) percentage of laser energy converted to THz and (d) average power transferred from the laser pulse to the plasma rescaled for fixed peak ponderomotive potential. Note that at $\tau = 50$ fs, these quantities do not match the results in Fig. 3.7 because the simulation length was shorter, and the damping rate ν was necessarily larger.

with τ for the same reason as $\langle P_r \rangle >$. The increase in the gradient of $\langle P_T \rangle >$ at small pulse lengths occurs because the bandwidth of plasma excitations increases rapidly as $\tau \to 0$, and so more energy is transferred to plasma waves. The increase in energy going into plasma waves means that less is available for THz radiation, which explains the peak seen in (a).

In Fig. 3.8(c) we see the ratio of $\langle P_r \rangle$ to $\langle P_T \rangle$, which we again interpret as the fraction of pulse energy that can be converted to THz radiation. As before, the combination of these two quantities result in a maximum, although this now occurs at $\tau \simeq 25$ ps. Thus, our previous choice of a 50 fs pulse did not result in the maximum THz generation. Fig. 3.8(d) contains the same results as (b), but rescaled so that the ponderomotive potential is fixed. The pulse energy is no longer constant, but its value for a 6 fs pulse is $U_0 = 0.01$ J. The purpose of this last plot is to verify that the results presented here are consistent with the fact that for fixed a_0, the maximum density perturbation occurs when the pulse duration matches the plasma period, which in this case is ~ 100 fs.

Now we present recorded values of the average radial power flow per unit frequency. We begin by studying the effect of different cutoff radii on the THz output, and then study the power spectrum as a function of density. The first set of results, seen in Fig. 3.9, are for channels with mode widths of $w_{ch} = 15$ μm and $w_{ch} = 50$ μm, both with an on-axis mean density is $n_0 = 10^{18}$ cm^{-3}. The cutoff function is found in Eq. (3.3), and we consider $1.5w_{ch} \leq r_c \leq 3.5w_{ch}$ and $r_0 - r_c = w_{ch}$. According to the discussion in Section 3.2, different values of r_c will result in different numbers of quasi-bound modes in the channel. The pulse length

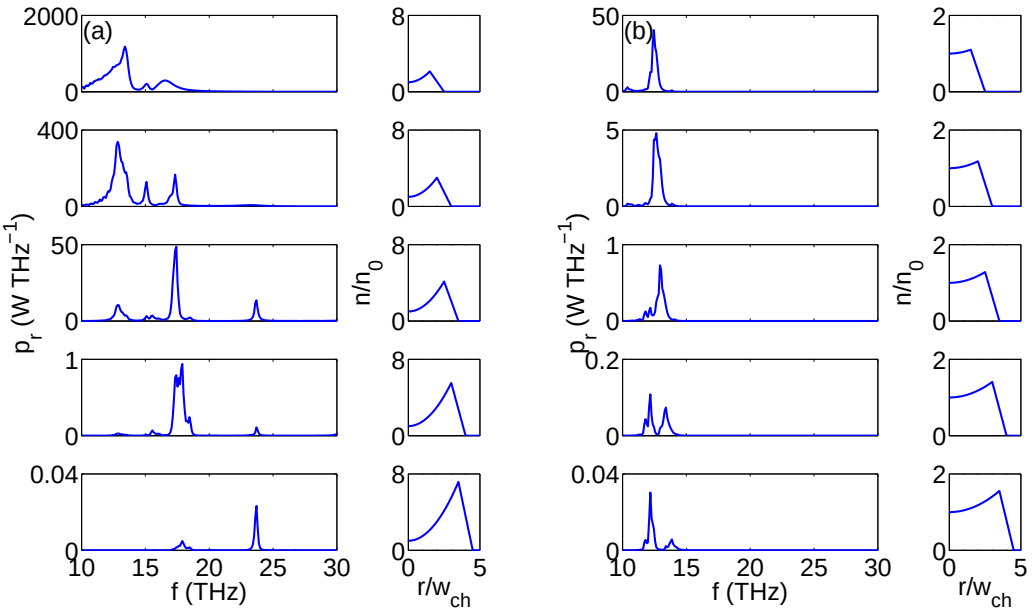

Figure 3.9: Average radial power spectral density for different cutoff radii and for corrugated channels with mode width (a) $w_{ch} = 15$ μm and (b) $w_{ch} = 50$ μm. The topmost plots have $r_c = 1.5w_{ch}$, and the cutoff radius increases by $.5w_{ch}$ for each successive plot. The subfigure to the right of each power plot displays a z-averaged radial density profile.

is once more 50 fs, and remaining parameters are the same as for previous results.

In Fig. 3.9(a) we see several different excitations. For $r_c = 1.5w_{ch}$ (top), there should only be one bound mode in the system, and so the visible excitations correspond to several different Floquet modes of the fundamental radial eigenmode. These excitations are somewhat broader than those for larger cutoff radius because for small r_c, the mode loses energy through the channel wall more rapidly. There is therefore a damping rate associated with the measured modes, and broadening occurs. For larger values of r_c we see higher frequency excitations. We will show later that the excitation at about 23 THz that appears for $r_c > 2.5w_{ch}$ is a second order radial eigenmode. The appearance of second order radial eigenmodes is consistent

with the number of modes we expect the channel the support, as calculated from Eq. (3.15).

Fig. 3.9(b) shows a single peak at about 12 THz for small values of r_c, and two peaks for larger cutoff radii. In this case, the frequency difference between successive Floquet modes is at most 3 THz, while the frequency difference between (the same Floquet excitation of) successive radial eigenmodes is at most 0.6 THz. These frequency differences are less than in the case of a smaller channel, and so while the excitations occur at around the expected frequency, we cannot claim them to be modes of a particular type and index.

We may study the excitations we see here in more detail by looking at the z-t Fourier transform of a field quantity measured outside the channel. This result is shown for the case $r_c = 2w_{ch}$ in Fig. 3.10, along with the lightline and a set of dispersion curves. We make this choice since this channel has one quasibound mode, but may still leak a significant amount of radiation. We can easily identify in these plots the modes seen in Fig. 3.9. We see at each excited frequency several different axial wavenumbers. These different wavenumbers come from the different spatial harmonics that comprise the Floquet modes, and as such they are separated by k_m. In vacuum these correspond to EM waves with wavevectors that are oblique to the z axis. The angle of propagation may be calculated using $\omega = |\boldsymbol{k}|c$. We note that for $k_z c > \omega$, there are no modes present. This is easily explained by considering the perpendicular wavenumber $k_\perp$, which outside the channel is given by

$$ck_\perp = \sqrt{\omega^2 - k_z^2 c^2}\ . \tag{3.34}$$

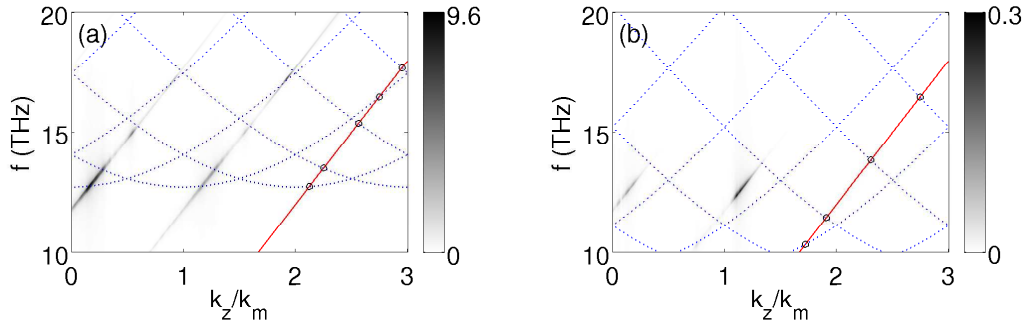

Figure 3.10: Two-dimensional Fourier transforms of E_z taken at fixed radius outside the channel for (a) $w_{ch} = 15$ μm and (b) $w_{ch} = 50$ μm. The red (solid) line is the lightline of the laser pulse, and the blue (dotted) curves are the functions in Eq. (3.10) that constitute the approximate dispersion relation.

The perpendicular wavenumber is imaginary for $|k_z c| > \omega$, and so these spatial harmonics are evanescent outside the channel boundary. Modes outside the channel boundary that have $|k_z c| \leq \omega$ have a real perpendicular wavenumber, and must therefore propagate away from the channel at an angle θ given by $\cos(\theta) = k_z c/\omega$. Since there are multiple spatial harmonics that satisfy the inequality for real $k_\perp$, we conclude that there will be a set of 'scattering' angles associated with each channel, and that the number of angles in this set will increase with density, increase with lightline-intersection number and decrease with mode width. These angles are given by

$$\theta = \arccos\left(1 - \frac{\beta k_m c}{\omega}\right) \qquad \beta = 0, 1, \ldots, \texttt{int}(2\omega/k_m c)\ . \tag{3.35}$$

The next set of results once again consists of values of the average radial power flow per unit frequency, this time recorded for a fixed value of $r_{ch} = 2w_{ch}$. This is done for mode widths of 15, 25, 50 and 75 μm, and densities ranging from 5×10^{17} cm^{-3} to 2.5×10^{18} cm^{-3}. The remaining parameters are the same as those used

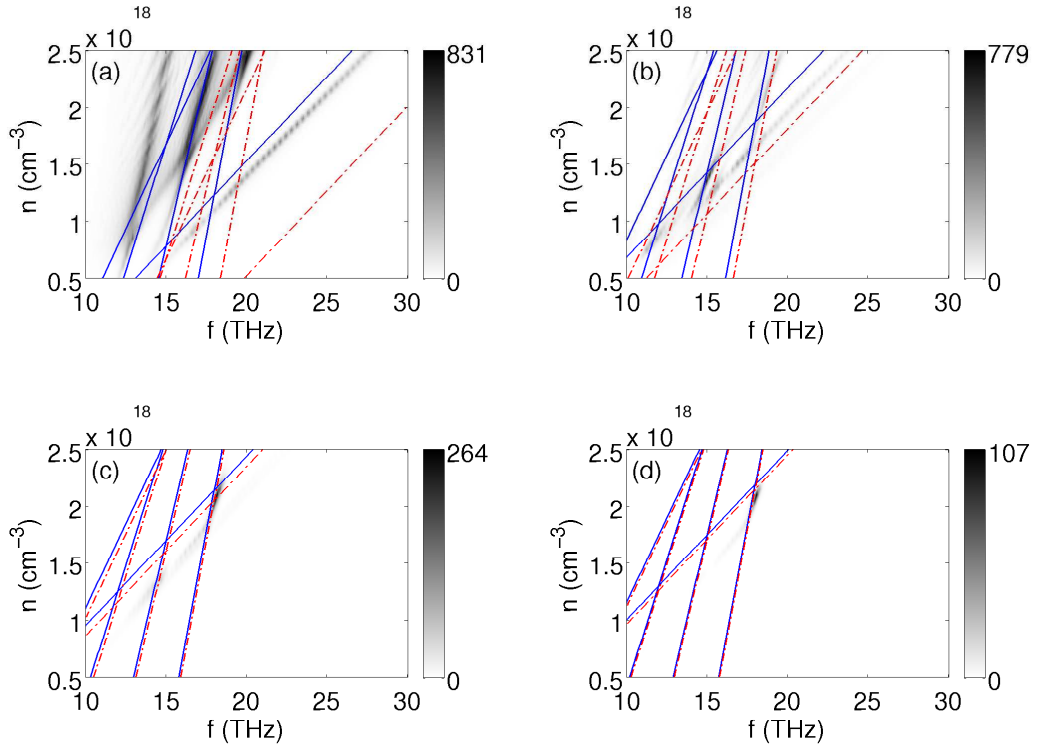

Figure 3.11: Plots of power density in frequency space as a function of density for channel widths (a) $w_{ch} = 15$ μm, (b) $w_{ch} = 25$ μm, (c) $w_{ch} = 50$ μm and (d) $w_{ch} = 75$ μm. The blue (solid) lines indicate the first five Floquet modes of the fundamental radial eigenmode, while the red (dot-dash) lines indicate the same for the second radial eigenmode, as predicted by the small δ theory.

previously to generate Fig. 3.9.

In Fig. 3.11 we see the variation of frequency of side-coupled radiation with density. For comparison, we plot the frequencies predicted by the small δ theory for the first five Floquet modes associated with the fundamental and second radial eigenmodes of the channel.

The fit is surprisingly good given our choice of $\delta = 0.9$. We explain this by considering the perturbative 'solution' to the Matthieu equation (i.e. assuming that coefficients A_α in Eq. (3.8) vanish for sufficiently large α). This solution yields a

finite number of dispersion curves with approximate bandgaps that range up to some maximum frequency and that are periodic in k out to some integer multiple of k_m. As we increase the perturbative order, the number of dispersion curves increases (increasing the range in ω), as does the number of periods in k over which they extend. Thus, since the excitations we observe come from the first few intersections of the lightline with the dispersion curves, which occur within the first few periods in k, a low order perturbative approximation should give an accurate result, with predictions far from the bandgaps being more accurate than those close to the bandgaps.

The gradient (dn/df) of the line corresponding to the lowest-numbered Floquet mode is significantly different than other Floquet modes. We see in Fig. 3.11(a) that this follows the excitation corresponding to the 17 THz peak in the second plot of Fig. 3.9(a) (this figure corresponds to a lineout of Fig. 3.11(a) at density $n = 10^{18}$ cm^{-3}.) Furthermore, the same line plotted for the second radial eigenmode is shifted to significantly higher frequency. Comparing this to the third figure in Fig. 3.9(a) suggests that the 23 THz excitation here is a second order radial eigenmode.

The general trend seen in Fig. 3.11(a) is for the power output to increase with density, which is consistent with the total power output results presented at the beginning of this section. The behavior is somewhat different for larger mode widths however. For Fig. 3.11(b), the peak output occurs at 15 THz at a density of about 1.4×10^{18} cm^{-3}, and at higher densities remains at a roughly constant level, albeit with a larger number of excitations. For Figures 3.11(c) and 3.11(d) the peak output occurs at 18 THz at a density of about 2×10^{18} cm^{-3} in both cases,

and is sufficiently pronounced that it is difficult to see any other excitations. Other excitations are present at a much lower level, as may be demonstrated with a plot of the logarithmic power output, seen in Fig. 3.12.

In many cases the peak excitations in Fig. 3.11 occur at or near an intersection of two frequency prediction lines generated by Eq. (3.11). We explain this by noting that an intersection in Fig. 3.11 corresponds to an intersection of the lightline in a dispersion plot constructed with functions of the form given in Eq. (3.10) at a point where two of these functions themselves intersect. An intersection in Fig. 3.11 therefore corresponds to a π or a 2π point, and we therefore expect to see strong excitations at some of them.

The presence of a dominant excitation from a single light line intersection for large mode widths, as opposed to many excitations for small mode widths, explains the features seen in Fig. 3.7(c) seen at the beginning of this section. For large mode widths, there are densities at which the conversion fraction f is a maximum, and it was shown that for an $\alpha = 1$ lightline intersection, these densities correspond to 2π points. We now see, upon examination of Figures 3.11(c) and 3.11(d), that this choice was justified. For smaller channels, we see many excitations corresponding to different lightline intersection numbers, and each will have a different 2π point density. Hence we expect that this will reduce the variation with density of the coupling, and so there won't be large variation with density in the conversion factor f. This is consistent with what is observed.

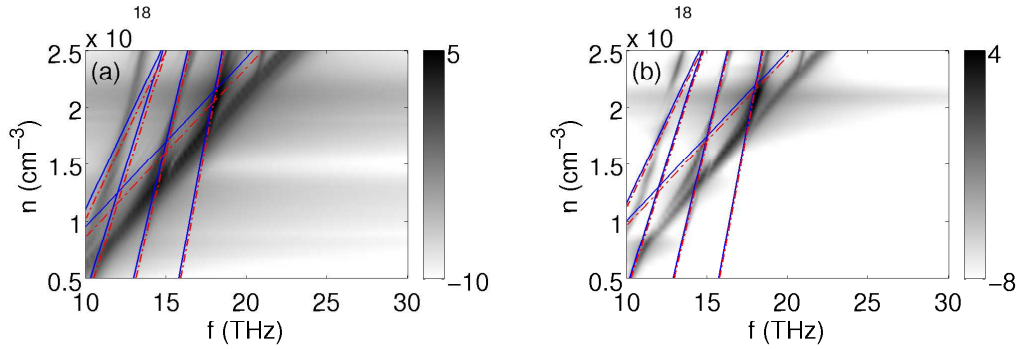

Figure 3.12: Log plots of power density in frequency space as a function of density for channel widths (a) $w_{ch} = 50$ μm and (b) $w_{ch} = 75$ μm. These demonstrate that the predicted frequencies are accurate for large channel widths also.

3.5 Conclusion

In conclusion, we have studied numerically the generation of THz radiation in a corrugated plasma channel. We have found that Terahertz modes are indeed excited, the reason being that the laser pulse can phase-match with the slow wave spatial harmonics supported by the channel. Some of these harmonics can then couple to free-space radiation modes on the side of the channel, with the angle of propagation being determined by the period in k_z in which the spatial harmonic wavenumber corresponding to the free space mode resides. Our results suggest that a significant fraction of the THz radiation power flow is radial, which is advantageous since these modes don't have to travel the length of the channel in order to escape. We haven't completely discounted the possibility of axial THz extraction however. We have also found that a small-density-modulation-amplitude approximation predicts THz radiation at frequencies similar to those observed in simulation results, despite the fact that the simulations were run with large modulation amplitudes.

We have found that the total radial power output is larger for smaller mode widths and for higher densities. The variation with mode width occurs because smaller mode widths lead to larger gradients of the ponderomotive potential, and because for fixed pulse energy, the peak ponderomotive potential increases with decreasing w_{ch}. The power output is larger for higher densities because the laser pulse drives larger currents and so does more work. We have found that THz is strongly emitted at certain angles corresponding to the axial wavenumbers of the different spatial harmonics, and we have found variation in power output with density due to the presence of π and 2π points in the dispersion relation. An experiment should therefore target the 'special' densities at which enhanced coupling occurs.

Finally, we have estimated the total fraction of laser pulse energy that is converted into THz to be around 1 percent for the densities and mode widths we considered. We have also shown for one set of channel parameters that the 50 fs pulse length is not optimum for generating THz, and that the ideal pulse is somewhat shorter. It appears, however, that this will not increase the pulse energy conversion fraction significantly. Extrapolating our results into the nonlinear regime, we obtain 6 mJ of THz from a .5 J pulse, with a linear depletion length of approximately twenty centimeters. This depletion length is for a 15 μm matched spot, and it increases significantly with spot size. Given experimental constraints, and the fact that the estimated THz power output assumes total pump depletion, we find that THz production requires small spot sizes.

A .5 J, 15 μm pulse has a normalized amplitude of $a_0 = 0.8$, and so pump

depletion will proceed in the weakly relativistic regime. Therefore, we treat the estimated depletion length as the upper bound to an effective depletion length over which most of the THz would be produced in a real system. The general conclusion is that a small spot, short pump pulse containing a significant fraction of a Joule, and a corrugated channel of several centimeters, is required to produce mJ-level amounts of THz radiation. Simulating such a system require a non-linear and relativistic analysis of pulse evolution in a corrugated plasma channel.

Appendix A

Calculating the Approximate Dispersion Relation

In calculating the mode structure in a corrugated plasma waveguide in Section 3.2, we encounter a one-dimensional ODE (Eq. (3.7)) which is related to the Matthieu equation. We construct a dispersion relation in the $\delta \to 0$ limit superimposing the dispersion curves for all of the different spatial harmonics of the solution, found in Eq. (3.8). This dispersion relation possesses the correct periodicity, but is somewhat inaccurate near the bandgaps. We note however that the results obtained from simulations in the $\delta \to 1$ limit match to some degree the approximate dispersion relation. The purpose of this appendix is to understand this result, and to quantify the differences between our dispersion relation and the exact result.

We begin by writing Eq. (3.9) in matrix form. The result is a vanishing product of a tridiagonal matrix and a vector of Fourier coefficients, i.e. $\mathsf{M} \cdot \boldsymbol{A} = 0$. Defining for brevity $\Omega_\alpha^2 = k_0^2 c^2 - (k_z - \alpha k_m)^2 c^2$, the dispersion relation (which is the condition for the existence of a non-trivial solution) is given by

$$\det(\mathsf{M}) = \begin{vmatrix} \ddots & \ddots & & & 0 \\ \ddots & 2\Omega_{\alpha-1}^2 & -i\omega_{p0}^2\delta & & \\ & i\omega_{p0}^2\delta & 2\Omega_\alpha^2 & -i\omega_{p0}^2\delta & \\ & & i\omega_{p0}^2\delta & 2\Omega_{\alpha+1}^2 & \ddots \\ 0 & & & \ddots & \ddots \end{vmatrix} = 0 \,. \tag{A.1}$$

We proceed by considering the strength of the coupling between Fourier coefficients A_α. For neighboring coefficients, we write this schematically as $A_\alpha \sim \epsilon A_{\alpha\pm1}$, and thus $A_\alpha \sim \epsilon^N A_{\alpha\pm N}$. If ϵ is small, we may choose to keep terms only to order ϵ^N, hence a particular Fourier coefficient will only be coupled to $2N$ of its neighbors, after which it will be decoupled. Because of this decoupling, our product $\mathsf{M}\cdot\boldsymbol{A}$ of an infinitely extended matrix and vector will reduce to an infinite number of products of a $(2N+1)\times(2N+1)$ matrix with a vector.

We need only evaluate the determinant of one of these matrices, since the dispersion curves resulting from the determinant centered around α will be related to those from the determinant centered around $\alpha+1$ by a translation of k_m. We note that this is exactly the procedure used to calculate the dispersion relation in Section 3.2, where we kept terms to order ϵ^0 and thus evaluated a 1×1 determinant.

In general, the small parameter ϵ depends on both δ, the modulation wavenumber k_m, and the frequency and wavenumber associated with the region of interest in the dispersion relation. Since we are interested in the region surrounding the first few lightline intersections, we have $\epsilon \sim \omega_{p0}^2\delta/\omega_c^2$. We may estimate the required size of the determinant using $2N+1 \sim 2\ln(\tau)/\ln(\epsilon)+1$, where τ is the desired fractional contribution of the most distantly coupled Fourier coefficient. For $\tau = 0.01$, we have for a $\delta = 0.9$, $n = 10^{18}$ cm^{-3}, $w_{ch} = 15$ μm channel a required determinant size of $2N+1 \sim 13$.

In Fig. A.1 we see dispersion curves plotted for $n = 10^{18}$ cm^{-3}, $\delta = 0.9$ and $w_{ch} = 15$ μm for various determinant sizes, including $N = 1$. In the $N = 1$ graph, we plot multiple dispersion curves to show a full dispersion relation, however for

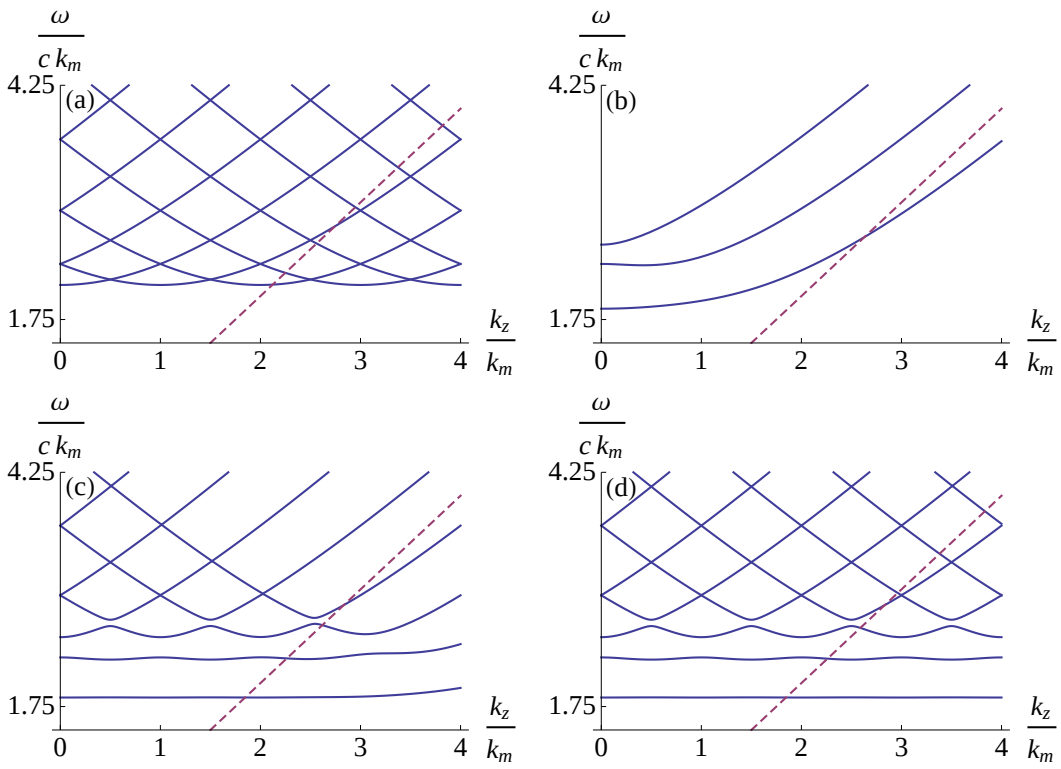

Figure A.1: Dispersion plots generated by evaluating a finite-sized version of the determinant shown in Eq. (A.1). Fig. (a) contains the dispersion construction discussed in Section 3.2, which is the dispersion relation from a single-element determinant reproduced many times. The remaining Figures contain dispersion curves calculated for (b) 3, (c) 9 and (d) 15 non-zero Fourier coefficients.

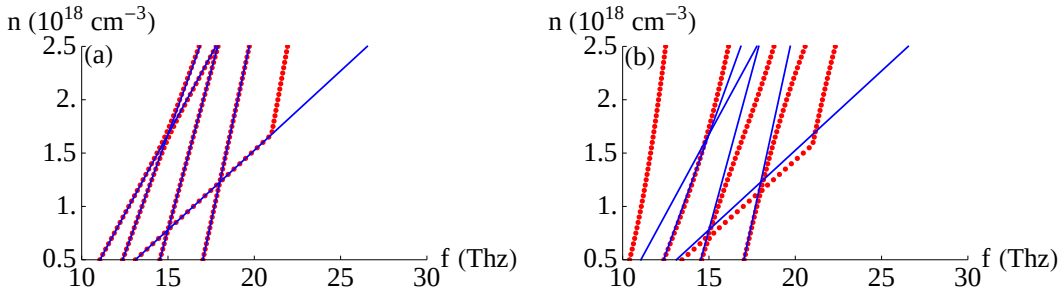

Figure A.2: Frequencies of lightline intersections with the dispersion curves in Fig. A.1(a) (blue, solid) and Fig. A.1(d) (red, dots) for (a) $\delta = 0.05$ and (b) $\delta = 0.9$. Note that the blue curves correspond to the solution presented in Eq. (3.11).

larger sizes, we plot only the solutions from a single determinant centered around $\alpha = 0$. We observe that as the number of non-zero Fourier coefficients increases, the number of individual curves increases, as does their extent in k_z space. We note however that the curve structure and bandgap size for small ω and k_z is accurate for much smaller truncation values than are necessary for correct curve structure at large ω and k_z.

We also note that the curve structure at large frequency very closely matches the piecewise dispersion relation, which explains why our simulation results conform so closely. For the case $\delta = 0.05$ (not shown), the large bandgaps that appear at low frequencies in the above plots reduce significantly, and the dispersion curves match the piecewise dispersion relation at low frequencies also.

Finally, we compare the frequencies generated by calculating the lightline intersections for the same density range as used in the simulations. These results are seen in Fig. A.2, and should be compared to the simulation results in Fig. 3.11(a).

Bibliography

[1] Henrik Stapelfeldt and Tamar Seideman. Colloquium: Aligning molecules with strong laser pulses. *Rev. Mod. Phys.*, 75(2):543–557, Apr 2003.

[2] Tamar Seideman and Edward Hamilton. *Nonadiabatic Alignment by Intense Pulses. Concepts, Theory, and Directions*, volume 52 of *Advances In Atomic, Molecular, and Optical Physics*, pages 289–329. Elsevier, 2005.

[3] Long Cai and Břetislav Friedrich. Recurring molecular alignment induced by pulsed nonresonant laser fields. *Collection of Czechoslovak Chemical Communications*, 66(7):991–1004, Unspecified 2001.

[4] Claude M. Dion, Arne Keller, Osman Atabek, and André D. Bandrauk. Laser-induced alignment dynamics of hcn: Roles of the permanent dipole moment and the polarizability. *Phys. Rev. A*, 59(2):1382–1391, Feb 1999.

[5] E. T. J. Nibbering, G. Grillon, M. A. Franco, B. S. Prade, and A. Mysyrowicz. Determination of the inertial contribution to the nonlinear refractive index of air, n2, and o2 by use of unfocused high-intensity femtosecond laser pulses. *J. Opt. Soc. Am. B*, 14(3):650–660, Mar 1997.

[6] F. Rosca-Pruna and M. J. J. Vrakking. Experimental observation of revival structures in picosecond laser-induced alignment of i_2. *Phys. Rev. Lett.*, 87(15):153902, Sep 2001.

[7] Y-H. Chen, S. Varma, A. York, and H. M. Milchberg. Single-shot, space- and time-resolved measurement of rotational wavepacket revivals in h2, d2, n2, o2, and n2o. *Opt. Express*, 15(18):11341–11357, 2007.

[8] P. W. Dooley, I. V. Litvinyuk, Kevin F. Lee, D. M. Rayner, M. Spanner, D. M. Villeneuve, and P. B. Corkum. Direct imaging of rotational wave-packet dynamics of diatomic molecules. *Phys. Rev. A*, 68(2):023406, Aug 2003.

[9] S. Ramakrishna and Tamar Seideman. Intense laser alignment in dissipative media as a route to solvent dynamics. *Physical Review Letters*, 95(11):113001, 2005.

[10] S. Ramakrishna and Tamar Seideman. Dissipative dynamics of laser induced nonadiabatic molecular alignment. *The Journal of Chemical Physics*, 124(3):034101, 2006.

[11] N Rostoker. Fluctuations of a plasma I. *Nuclear Fusion*, 1(2):101–120, 1961.

[12] Nicholas A. Krall and Alvin W. Trivelpiece. *Principles of Plasma Physics*. McGraw-Hill New York, 1973.

[13] Gilbert Cooper. Shielding of slow test particles in a plasma. *Physics of Fluids*, 12(12):2707–2710, 1969.

[14] J. R. Cash and Alan H. Karp. A variable order runge-kutta method for initial value problems with rapidly varying right-hand sides. *ACM Trans. Math. Softw.*, 16(3):201–222, 1990.

[15] C. H. Townes and A. L. Schawlow. *Microwave Spectroscopy*. McGraw-Hill Book Company, 1955.

[16] J. O. Hirschfelder, C. F. Curtiss, and R. B. Bird. *Molecular Theory of Gases and Liquids*. Wiley, New York, 1954.

[17] G. Herzberg. *Molecular Spectra and Molecular Structure : Volume I-Spectra of Diatomic Molecules, 2nd ed.* Krieger Malabar, FL, 1989.

[18] A. Crocker. Stimulated Emission in the Far Infra-Red. *Nature*, 201:250–251, January 1964.

[19] Jerome Faist, Federico Capasso, Deborah L. Sivco, Carlo Sirtori, Albert L. Hutchinson, and Alfred Y. Cho. Quantum Cascade Laser. *Science*, 264(5158):553–556, 1994.

[20] D. H. Auston, K. P. Cheung, J. A. Valdmanis, and D. A. Kleinman. Cherenkov radiation from femtosecond optical pulses in electro-optic media. *Phys. Rev. Lett.*, 53(16):1555–1558, Oct 1984.

[21] Ch. Fattinger and D. Grischkowsky. Terahertz beams. *Applied Physics Letters*, 54(6):490–492, 1989.

[22] Zhiping Jiang and Xi-Cheng Zhang. Terahertz imaging via electrooptic effect. *Microwave Theory and Techniques, IEEE Transactions on*, 47(12):2644 –2650, dec 1999.

[23] A. Staprans, E.W. McCune, and J.A. Ruetz. High-power linear-beam tubes. *Proceedings of the IEEE*, 61(3):299 – 330, march 1973.

[24] Steven H. Gold and Gregory S. Nusinovich. Review of high-power microwave source research. *Review of Scientific Instruments*, 68(11):3945–3974, 1997.

[25] Gerald Ramian. The new ucsb free-electron lasers. *Nuclear Instruments and Methods in Physics Research Section A: Accelerators, Spectrometers, Detectors and Associated Equipment*, 318(1-3):225 – 229, 1992.

[26] K. W. Berryman, E. R. Crosson, K. N. Ricci, and T. I. Smith. Coherent spontaneous radiation from highly bunched electron beams. *Nuclear Instruments and Methods in Physics Research Section A: Accelerators, Spectrometers, Detectors and Associated Equipment*, 375(1-3):526 – 529, 1996. Proceedings of the 17th International Free Electron Laser Conference.

[27] V.P. Bolotin, N.A. Vinokurov, D.A. Kayran, B.A. Knyazev, E.I. Kolobanov, V.V. Kotenkov, V.V. Kubarev, G.N. Kulipanov, A.N. Matveenko, L.E. Medvedev, S.V. Miginsky, L.A. Mironenko, A.D. Oreshkov, V.K. Ovchar, V.M. Popik, T.V. Salikova, S.S. Serednyakov, A.N. Skrinsky, O.A. Shevchenko, and M.A. Scheglov. Status of the novosibirsk terahertz fel. *Nuclear Instruments and Methods in Physics Research Section A: Accelerators, Spectrometers, Detectors and Associated Equipment*, 543(1):81 – 84, 2005. Proceedings of the XV International Synchrotron Radiation Conference.

[28] W. P. Leemans, C. G. R. Geddes, J. Faure, Cs. Tóth, J. van Tilborg, C. B. Schroeder, E. Esarey, G. Fubiani, D. Auerbach, B. Marcelis, M. A. Carnahan, R. A. Kaindl, J. Byrd, and M. C. Martin. Observation of terahertz emission from a laser-plasma accelerated electron bunch crossing a plasma-vacuum boundary. *Phys. Rev. Lett.*, 91(7):074802, Aug 2003.

[29] H. Hamster, A. Sullivan, S. Gordon, W. White, and R. W. Falcone. Subpicosecond, electromagnetic pulses from intense laser-plasma interaction. *Phys. Rev. Lett.*, 71(17):2725–2728, Oct 1993.

[30] J. Yoshii, C. H. Lai, T. Katsouleas, C. Joshi, and W. B. Mori. Radiation from cerenkov wakes in a magnetized plasma. *Phys. Rev. Lett.*, 79(21):4194–4197, Nov 1997.

[31] W. P. Leemans, J. van Tilborg, J. Faure, C. G. R. Geddes, Cs. Toth, C. B. Schroeder, E. Esarey, G. Fubiani, and G. Dugan. Terahertz radiation from laser accelerated electron bunches. *Physics of Plasmas*, 11(5):2899–2906, 2004.

[32] B. D. Layer, A. York, T. M. Antonsen, S. Varma, Y.-H. Chen, Y. Leng, and H. M. Milchberg. Ultrahigh-intensity optical slow-wave structure. *Phys. Rev. Lett.*, 99(3):035001, Jul 2007.

[33] Thomas. M. Antonsen, John Palastro, and Howard M. Milchberg. Excitation of terahertz radiation by laser pulses in nonuniform plasma channels. *Physics of Plasmas*, 14(3):033107, 2007.

[34] Jr. Thomas M. Antonsen. Radiation generated by bunched electron beams in corrugated plasma channels. *Physics of Plasmas*, 17(7):073112, 2010.

[35] J. P. Palastro, T. M. Antonsen, S. Morshed, A. G. York, and H. M. Milchberg. Pulse propagation and electron acceleration in a corrugated plasma channel. *Phys. Rev. E*, 77(3):036405, Mar 2008.

[36] B. A. Shadwick, C. B. Schroeder, and E. Esarey. Nonlinear laser energy depletion in laser-plasma accelerators. *Physics of Plasmas*, 16(5):056704, 2009.

[37] A. Ting, E. Esarey, and P. Sprangle. Nonlinear wake-field generation and relativistic focusing of intense laser pulses in plasmas. *Physics of Fluids B: Plasma Physics*, 2(6):1390–1394, 1990.

[38] John D. Jackson. *Classical Electrodynamics Third Edition*. Wiley, 3 edition, August 1998.

[39] Patrick Mora and Thomas M. Antonsen. Kinetic modeling of intense, short laser pulses propagating in tenuous plasmas. *Physics of Plasmas*, 4(1):217–229, 1997.

[40] Kane Yee. Numerical solution of initial boundary value problems involving maxwell's equations in isotropic media. *Antennas and Propagation, IEEE Transactions on*, 14(3):302 –307, May 1966.

[41] NVidia. CUDA GPUs. `http://www.nvidia.com/object/cuda_gpus.html`.

[42] Jean-Pierre Berenger. A perfectly matched layer for the absorption of electromagnetic waves. *Journal of Computational Physics*, 114(2):185 – 200, 1994.